SLAC-PUB-2625
October 1980
(T/E)

DEEP INELASTIC PHENOMENA*

C. Y. Prescott

Stanford Linear Accelerator Center,
Stanford University, Stanford, California 94305

TABLE OF CONTENTS

I. INTRODUCTION

In these two lectures I will review and bring up to date our picture of nucleon structure as seen in the context of deep inelastic scattering. From the very early days of inelastic scattering to the present, this subject has been continually reviewed by many persons. As the data have expanded over wider kinematic territory, and as the theoretical framework has expanded and improved,

*Work supported by Department of Energy, contract DE-AC03-76SF00515.
(Invited talk at XVIII International School of Subnuclear Physics, Ettore Majorana, Erice, Italy, July 31 - August 11, 1980.)

the questions we are asking have changed as well. The lectures begin with consideration of the quark-parton model. The model forms the basis of our understanding of lepton-nucleon inelastic scattering. This model is weak on formal, theoretical justification, but very strong on intuitive understanding of the processes. As improved data in lepton-nucleon scattering at high energies became available, the quark-parton model failed to explain some crucial features of these data. At approximately the same time a candidate theory of strong interactions based on a SU(3) gauge theory of color was being discussed in the literature, and new ideas on the explanation of inelastic scattering data became popular. A new theory of strong interactions, now called quantum chromodynamics provides a new framework for understanding the data, with a much stronger theoretical foundation, and seems to explain well the features of the data. Although there are many problems yet to be resolved, both in the data and in the QCD calculations, one is impressed at the qualitative level by the QCD-like features seen in the data taken as a whole. The lectures will conclude with a look at some recent experiments which provide new data at very high energies. These lectures are concerned primarily with charged lepton inelastic scattering and to a lesser extent with neutrino results. Furthermore, due to time and space limitations, topics such as final state hadron studies, and multi-muon production are omitted here. The lectures concentrate on the more central issues: the quark-parton model and concepts of scaling, scale breaking and the ideas of quantum chromodynamics, the Q^2 dependence of structure function, moments, and the important parameter R.

II. THE QUARK-PARTON MODEL AND SCALING

Figure 1 shows the basic process under consideration. An incident lepton ℓ scatters at a laboratory angle θ from a stationary nucleon. The nucleon fragments into a recoiling state X, of invariant mass W, not specifically identified.

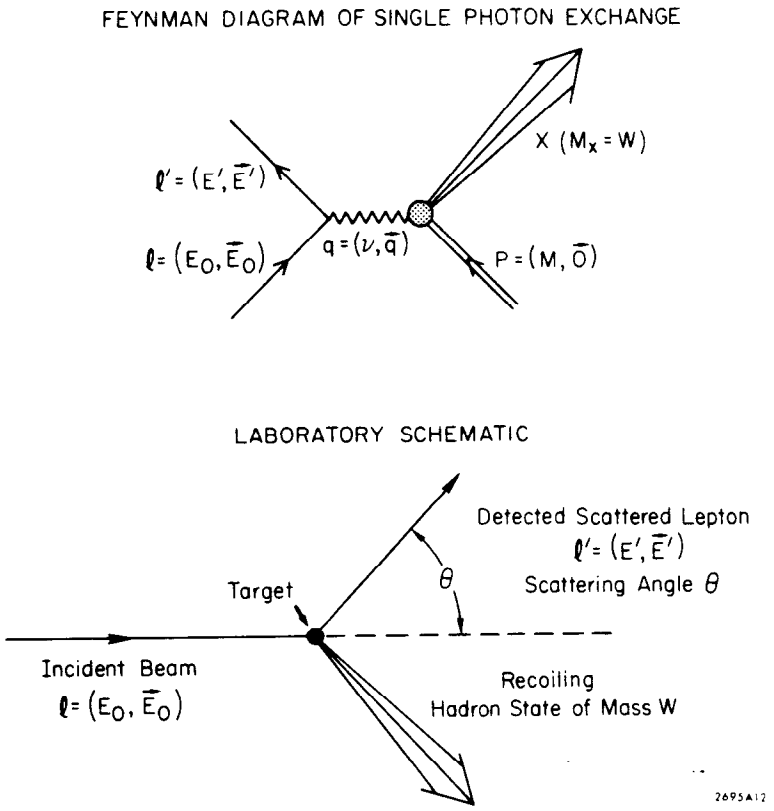

Fig. 1. Dynamics and kinematic variables in lepton-nucleon scattering.

Figure 1 shows the dynamical picture; for charged lepton scattering a single virtual photon transmits the force from lepton to hadrons. For neutrino interactions, the photon is replaced by $W^{\pm}$ or Z^{o}. Kinematic parameters are important in any discussion of features of the data. Definition of the commonly used variables are:

$$Q^2 = -\left(\ell_\mu - \ell'_\mu\right)^2 = 4E_0E' \sin^2\frac{\theta}{2} \tag{1}$$

where Q^2 is the invariant four momentum transfer-squared, E_0 is the incident lepton energy, and E' is the outgoing lepton energy.

$$W^2 \equiv M_x^2 = \left(p_\mu + q_\mu\right)^2 = M^2 + 2M\left(E_0 - E'\right) - Q^2 \tag{2}$$

is the invariant mass squared of the final state hadrons.

$$\nu = E_0 - E' \tag{3}$$

is the energy lost by the lepton and transferred to the hadrons.

$$x = \frac{Q^2}{2M\nu} \qquad \text{and} \qquad y = \frac{\nu}{E_0} \tag{4}$$

are scaling variables with special meaning in the quark-parton model. For elastic scattering, $W^2 = M^2$, which by equation (2) gives $2M\nu = Q^2$, and $x = 1$. These relations for elastic scattering will be important.

The quark-parton model was introduced in 1969 by Richard Feynman[1] as an intuitive explanation of scaling predicted by J. D. Bjorken[2] and exhibited by the early inelastic electron scattering data from SLAC.[3] The picture Feynman introduced is shown in Fig. 2 where a virtual photon scatters off a quasi-free constitutent which carries a fraction ξ of the target particle momentum P. Target mass effects, constituent mass effects, interactions between the constituents, and transverse momentum of the constituents are ignored. Elastic scattering from such a quasi-free constituent of mass m carrying a fraction ξ of the nucleon's momentum gives

$$\left(\xi p_\mu + q_\mu\right)^2 = m^2 \tag{5}$$

or

$$\xi M^2 + 2M\nu\xi - Q^2 = m^2 \ .$$

Solving for the fraction ξ gives

$$\xi = \frac{Q^2 + m^2}{M\left(\nu + \sqrt{\nu^2 + Q^2 + m^2}\right)} \tag{6}$$

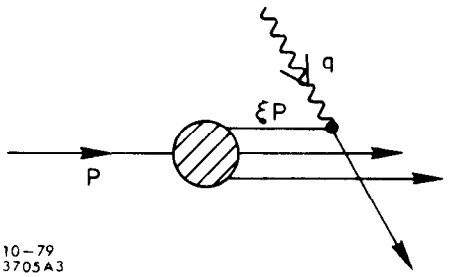

10-79
3705A3

Fig. 2. Virtual photon scattering from a nucleon constituent

For $\nu^2 >> Q^2 >> m^2$, we find a simple form for ξ, first introduced by Bjorken (the Bjorken scaling limit)

$$\xi = x = \frac{Q^2}{2M\nu} \tag{7}$$

The relation $x = Q^2/2M\nu$ has interesting physical consequences. The ratio $Q^2/2M\nu$ determines the fraction of the total momentum carried by parton involved in the scattering event. It can be obtained solely from the scattering kinematics of the leptonic side of the reaction. Suppose the nucleon consisted of only two partons which carried fractional momentum x_1 and x_2. Then the scattering of leptons would occur only for two values of $Q^2/2M\nu$, namely x_1 and x_2, although Q^2 and ν would vary. This is the constraint imposed by elastic scattering from each of the massless partons. If the nucleon consisted of a distribution of partons of momenta x_i, then scattering of leptons would be seen for a distribution of values of $Q^2/2M\nu = x_i$. The distribution in x of inelastic scattering events, corrected for kinematic factors, can be related to the probability of finding a parton of fractional momentum x contributing to the scattering.

Elastic scattering can be considered an example of parton scattering where only one constituent exists. Equation (2), with W set to M, gives $Q^2/2M\nu = 1$, agreeing with the picture that a single constituent of the nucleon must carry the total momentum. Cross section formulae for elastic scattering from nucleons are expressed in terms of form factors, which depend on a single kinematic variable, Q^2. In the case of inelastic scattering, similar form factors exist, called "structure functions", but in general these form factors are functions of two variables, Q^2 and ν. In the parton model the inelastic scattering arises from elastic scattering from point particles and these structure functions will depend only on a single variable, x. This simplification in the form of the hadronic part of the cross section carries the name "scaling", and represents simply a kinematic constraint resulting from elastic scattering

from quasi-free constituents.

Another variable of considerable importance to inelastic scattering phenomenology is the parameter y. In Fig. 3, the scattering from a constituent quark is shown in the CMS system and in the lab. Boosting from the CMS to the lab gives for the outgoing lepton energy, neglecting masses,

$$E' = \gamma(E^* + \beta E^* \cos\theta^*)$$

$$\simeq \frac{E_0}{2}(1 + \cos\theta^*)$$

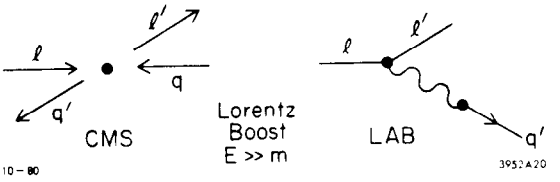

Fig. 3. Lepton-quark scattering in two frames.

or

$$\frac{E'}{E_0} = \tfrac{1}{2}(1 + \cos\theta^*) \quad . \qquad (8)$$

Since

$$y = \frac{E_0 - E'}{E_0}$$

$$(1 - y) = \tfrac{1}{2}(1 + \cos\theta^*) \quad . \qquad (9)$$

We observe that y is related to the CMS scattering angle of the lepton in the lepton-quark system. The parameter y is readily measured in high energy experiments, and the factor (1 - y) will take on special significance in quark-parton model descriptions of the scattering process, as will be described later.

The choice of an appropriate scaling variable for describing the data has been a subject of discussion from the early days of scaling. The original scaling variable of Bjorken's, $x = Q^2/2M\nu$, applied to asymptotic energies, and no guidance was given regarding use of x to test scaling at low energies and for targets of finite mass.

Figure 4 shows the behavior of one of the two nucleon structure functions, $F_2^{ep}(x,Q^2)$, plotted in the variable x. The data are from SLAC/MIT data sets and include a broad range of Q^2, from 2 GeV^2 to

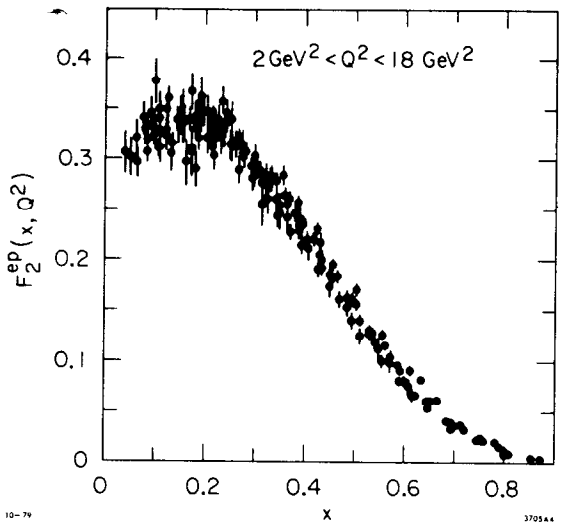

Fig. 4. Proton structure function F_2 derived from electron-proton scattering.

18 GeV^2. Scaling of the data implies that F_2^{ep} at fixed x will be independent of Q^2. Figure 4 shows quite clearly the scaling nature of the data. All data fall into a narrow range whose value depends on x, but appears to be nearly independent of Q^2. The fact that the scaling nature sets in early at low energies, well below the Bjorken limit, led to the phrase "precocious scaling" associated with these data.

Scaling in these data is only approximate, as indicated by the band of data points which appears to be wider than the errors permit. Even in the early days of inelastic scattering data, deviations from exact scaling were evident. One explanation of the small deviations from exact scaling was that mass effects were neglected in the choice of scaling variables. New scaling variables were introduced, for example

$$x' = \frac{Q^2}{(2M\nu + M^2)} \tag{10}$$

by G. Miller[4] and

$$\xi = \frac{2x}{\left(1 + \sqrt{1 + \frac{4M^2x^2}{Q^2}}\right)} \tag{11}$$

by Breidenbach and Kuti and later Nachtmann.[5] The variable ξ incorporated target mass terms and was shown to improve the scaling behavior of the low energy data when substituted for x.

In deep inelastic scattering, the hadronic part of the interaction is decomposed into two pieces, representing a particular

choice of the two inelastic form factors called "structure functions". These two structure functions are now most commonly denoted $F_1^{eN}(x,Q^2)$ and $F_2^{eN}(x,Q^2)$, where the superscript eN refers to the reaction in which they occur. Structure functions for μN inelastic scattering and νN inelastic scattering are expected to be closely related to those for eN.

The cross section for $eN \to eX$, in terms of the kinematic parameters and F_1 and F_2 is given by

$$\frac{d^2\sigma}{dQ^2dx} = \frac{4\pi\alpha^2}{Q^4}\left[\left(1 - y - \frac{Mxy}{2E_0}\right)\frac{F_2^{eN}(x,Q^2)}{x} + \frac{y^2}{2}\,2F_1^{eN}(x,Q^2)\right] \quad (12)$$

which serves, for the purpose of these lectures, to define the nucleon structure functions F_1 and F_2. One can show for elastic scattering from point-like spin-½ targets of charge Z_i,

$$\frac{d\sigma}{dQ^2} = \frac{4\pi\alpha^2}{Q^4}\left[\left(1 - y - \frac{My}{2E_0}\right) + \frac{y^2}{2}\right] Z_i^2 \quad (13)$$

which suggests (in the limit $E_0 >> m$)

$$2xF_1(x,Q^2) = F_2(x,Q^2) \quad (14)$$

This relation, known as the Callan-Gross relation[6] is closely related to a parameter R, predicted to be zero in the Bjorken limit, which will be discussed in some detail in the next lecture. The Callan-Gross relation is almost exact in eN inelastic scattering and in νn inelastic scattering. Small deviations are observed in eN data, and in the most recent νN data small deviations from exact Callan-Gross behavior also appear to occur. The Callan-Gross relation is important because it is nearly satisfied by the data and indicates the spin-½ nature of the constituents, but also because it can be used to eliminate one of the structure functions (usually F_1) in the phenomenological analysis of the data. The Callan-Gross relation is often assumed because of the simplification of form it brings.

Inelastic scattering of neutrinos off nucleons has a somewhat more complicated structure than eN or μN scattering. The weak interactions couple through both vector couplings (V) and axial-vector couplings (A), which lead to a third structure function F_3. The complete form of the cross section for inelastic neutrino scattering is

$$\frac{d^2\sigma^{\nu,\bar{\nu}}}{dxdy} = \frac{G^2}{\pi} ME_0 \left[\left(1-y-\frac{Mxy}{2E_0}\right) F_2^{\nu N}(x,Q^2) + \frac{y^2}{2} \pm y\left(1-\frac{y}{2}\right) xF_3^{\nu N}(x,Q^2) \right] \quad (15)$$

which serves to define phenomenologically $F_1^{\nu N}(x,Q^2)$, $F_2^{\nu N}(x,Q^2)$ and $F_3^{\nu N}(x,Q^2)$. The +(-) sign in the F_3 term refers to $\nu(\bar{\nu})$ cross section.

The charged current neutrino interactions are helicity dependent due to the V-A nature of the vertices. Only neutrinos and quarks of negative helicity interact, while for anti-neutrinos and anti-quarks, the charged weak currents pick out positive helicity. Figure 5 illustrates the contributions to the cross sections. Consider a target nucleon consisting of a mixture of quarks and anti-quarks. Neutrino scattering off quarks proceeds by the $J_z = 0$ component of the weak current. The center-of-mass angular distribution for $J_z = 0$ currents is a constant, and the corresponding y-distribution is flat. For neutrinos interacting on anti-quarks, the interaction proceeds through a $J_z = -1$ component, resulting in a $(1+\cos\theta^*)^2$ angular distribution and y-distribution of the form $(1-y)^2$ from equation (9).

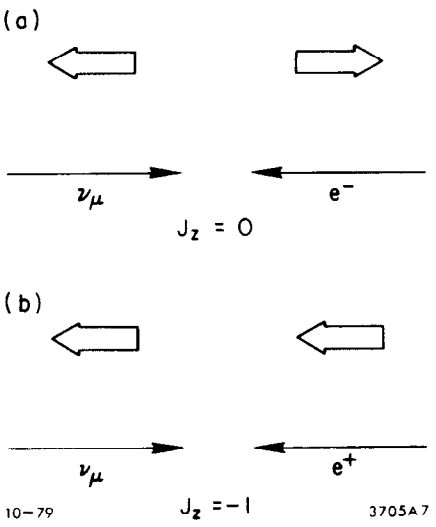

Fig. 5. Helicity restrictions in neutrino scattering from spin-½ particles.

If one defines a quark distribution q(x) to represent the probability of finding a quark q with a

fraction of momentum x, and $\bar{q}(x)$ to represent the probability of finding an anti-quark $\bar{q}$ with a fraction of momentum x, then the neutrino cross section has the form

$$\frac{d^2\sigma^{\nu}}{dxdy} = \frac{2G^2}{\pi} xME_0 \left\{ q(x) + (1-y)^2 \bar{q}(x) \right\} \tag{16a}$$

and the anti-neutrino cross section has the form

$$\frac{d^2\sigma^{\bar{\nu}}}{dxdy} = \frac{2G^2}{\pi} xME_0 \left\{ \bar{q}(x) + (1-y)^2 q(x) \right\} . \tag{16b}$$

Assuming that the Callan-Gross relation is valid and using it to eliminate $2xF_1$, equations (15) and (16) give

$$F_2^{\nu N}(x,Q^2) = 2x \left\{ q(x,Q^2) + \bar{q}(x,Q^2) \right\} \tag{17}$$

and

$$xF_3^{\nu N}(x,Q^2) = 2x \left\{ q(x,Q^2) - \bar{q}(x,Q^2) \right\} . \tag{18}$$

The quantity $xq(x,Q^2)$ is the momentum carried by quarks of fractional momentum x, and integrals of F_2 represent the total momentum carried by quarks and anti-quarks. In a model of the nucleon where anti-quarks come from quark - anti-quark pairs out of a "sea", in analogy to virtual electron-positron pairs found in the vicinity of a Coulomb field, then $xF_3/2x$ represents the excess of quarks over anti-quarks in the nucleon. The integral of $xF_3/2x$ is expected to equal 3 for a nucleon consisting of 3 valence quarks plus a quark - anti-quark symmetric sea.

The y-distributions in ν and $\bar{\nu}$ inelastic scattering reveal the quark and anti-quark content of the nucleon. Figure 6 shows cross section data for ν and $\bar{\nu}$ beams. The y-distributions are fit to a constant and a $(1-y)^2$ term coming from the smaller anti-quark content. The anti-neutrino cross section on the other hand has a large $(1-y)^2$ term in agreement with the large quark content of

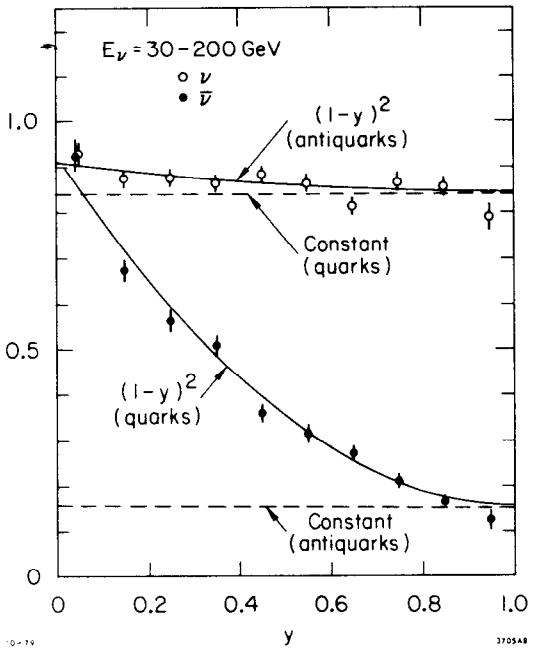

Fig. 6. y-distributions for neutrino and anti-neutrino nucleon scattering.

the nucleon. These data show quite clearly the presence of both quarks and anti-quarks in the nucleon.

Suppose the nucleon consists of u, d, s and c quarks and their corresponding anti-quarks $\bar{u}$, $\bar{d}$, $\bar{s}$ and $\bar{c}$. Then

$$F_2^{\nu N}(x) = 2x\{u(x) + \bar{u}(x) + d(x) + \bar{d}(x) + \ldots\} \quad (19)$$

where $q(x,Q^2)$ has been expanded into its various flavor components, and Q^2 has been dropped for simplicity, but in principle still belongs in these functions.

The corresponding form of equation (19) for eN or μN scattering must contain the charge-weighted distributions

$$F_2^{eN}(x) = \sum z_i^2 \, x\left(q_i(x) + \bar{q}_i(x)\right)$$

Expanding this for the proton and neutron

$$F_2^{ep}(x) = x\left\{\frac{4}{9}\left(u_p(x)+\bar{u}_p(x)\right) + \frac{1}{9}\left(d_p(x)+\bar{d}_p(x)\right) + \ldots\right\}$$

$$F_2^{en}(x) = x\left\{\frac{4}{9}\left(u_n(x)+\bar{u}_n(x)\right) + \frac{1}{9}\left(d_n(x)+\bar{d}_n(x)\right) + \ldots\right\} \quad . \quad (20)$$

Using isospin rotation, which takes n ↔ p and u ↔ d, we have

$$u_n(x) = d_p(x) \text{ and } d_n(x) = u_p(x) \; .$$

$$F_2^{en}(x) = x\left\{\frac{4}{9}\left(d_p(x) + \bar{d}_9(x)\right) + \frac{1}{9}\left(u_p(x) + \bar{u}_p(x)\right) + \ldots\right\}$$

Averaging over ep and en for an isoscalar target, and neglecting heavy quarks gives

$$F_2^{eN}(x) \simeq \frac{5}{18} F_2^{\nu N} \quad . \tag{22}$$

This approximate relation is often used to compare eN or μN and νN data. This relation seems to be closely satisfied by the data, and therefore lends strong support for the quark-parton picture of nucleon structure.

A quantity similar to xF_3^N of equation 18, is $F_2^{ep} - F_2^{en}$ from inelastic electron scattering. In the quark-parton model, the $q\bar{q}$ sea terms are the same for the proton and neutron, while valence quark contributions are different. Thus the difference $F_2^{ep} - F_2^{en}$ picks out the valence quark contributions. Figure 7 shows two examples of scattering from nucleon constituents. The first trivial example shows elastic ep scattering, which occurs at $x = 1$, broadened by experimental resolution and radiative processes. The second example is more interesting. It shows $F_2^{ep} - F_2^{en}$ distributions in x, but with arbitrary normalization. The distribution peaks at $x \simeq 1/3$, corresponding to a most probable momentum for the valence quarks of 1/3 of the total. This is evidence that there are three valence quarks in the nucleon.

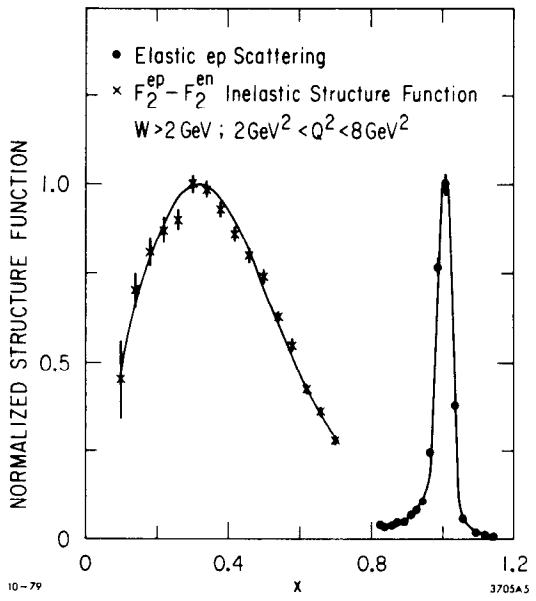

Fig. 7. Examples of elastic and inelastic electron-nucleon scattering.

No discussion of scaling and nucleon structure is complete without some mention of sum rules. Sum rules have provided a great deal of important conclusions about the validity of the quark-parton model. It can be shown that for incoherent scattering off free constituents,

$$\int_0^1 \frac{F_2^{ep}(x)}{x}\,dx = \sum_i z_i^2 \tag{23}$$

This is known as the Gottfried sum rule. For a proton of two u quarks and one d quark, $\sum z_i^2 = 1$. The experimental value, measured in ep data is

$$\int_{.02}^{.82} \frac{F_2^{ep}(x)}{x}\,dx = 1.05 \pm .09 \tag{24}$$

The integral is sensitive to the form of $F_2(x)$ at small x, so the interpretation of the experimental value could be challenged, but at first glance, it is consistent with a simple valence quark model of the nucleon. Another sum rule is

$$\int_0^1 \frac{xF_3(x)}{x}\,dx = 2\int_0^1 \sum_i \left(q_i(x) - \bar{q}_i(x)\right) dx \quad . \tag{25}$$

This integral is the Gross-Llewellyn-Smith sum rule, and is expected to have a value of six for three valence quarks. The measured value is 6.4 ± 1 from CDHS neutrino data. These two sum rules are consistent with the quark-parton picture of the nucleon containing three valence quarks and a sea of quark - anti-quark pairs.

Finally, a third and very important sum rule,

$$\int_0^1 F_2^{ep}(x)\,dx = \int_0^1 \sum_i z_i^2\, x\left(q_i(x) + \bar{q}_i(x)\right) dx \tag{26}$$

is known as the momentum sum rule. For a simple proton consisting

of two u quarks and one d quark, each carrying 1/3 of the momentum,

$$\int_0^1 \sum_i z_i^2 \, xq_i(x) \, dx = 1/3 \quad .$$

The experimentally measured value is

$$\int_0^1 F_2^{ep}(x) \, dx \simeq .15 \tag{27}$$

Here we see a significant deviation from the simple quark-parton model. If one looks at νN data, the corresponding momentum sum rule gives

$$\int_0^1 F_2^{\nu N}(x) \, dx \simeq .5 \tag{28}$$

where one expects 1. In both cases, there appears to be missing momentum based on the quark-parton model interpretation of the meaning of F_2. Inelastic νN and eN agree that approximately one half of the momenta is missing, and the interpretation is that there are neutral constituents in the nucleon. That is, there must reside in the nucleon constituents that carry momenta, but carry neither electromagnetic or weak charge. This is one piece of evidence that the simple quark-parton picture of the nucleon is not valid. We have already seen residual evidence of scale-breaking features in the structure functions. The fact that the parton-model description ignored the possibility of strong interaction effects in the hadrons left the description somewhat incomplete. Perhaps most disconcerting, at least to some subset of the physicists, was the lack of a rigorous foundation to the parton model. A candidate theory of strong interactions was emerging which could at least bypass the latter problem. A gauge theory of colored gluons and quarks was being developed which could be applied to deep inelastic scattering. In the final analysis there now seems to be compelling reasons to go to

such a theory, at least as a replacement to the parton model. The most important of these is the rigorous formal basis for the theory, and the simple fact. as we shall see, that it appears to describe well the data. Therefore, I would now like to turn to the questions of quantum chromodynamics, as this theory is called. I will discuss the underlying intuitive ideas, and the phenomenology as it applies to deep inelastic scattering. But let me emphasize here that quantum chromodynamics does not replace the quark-parton model in inelastic scattering. Instead the description of deep inelastic scattering incorporates the older quark-parton model ideas and QCD extends it to include quark-quark interactions.

III. SCALE BREAKING AND QUANTUM CHROMODYNAMICS

Quantum chromodynamics is a gauge field theory of colored gluons and colored quarks. The strong force is mediated by massless vector particles called gluons which couple to a strong charge called color. Gluons carry color, quarks carry color, but leptons do not. There is a fundamental coupling constant α_s which represents the strength of coupling at the quark-gluon and gluon-gluon vertices. It's symbol α_s reflects the analogy to the fine structure constant of quantum electrodynamics. In Fig. 8 we see the three basic diagrams in the dynamics. They are labelled "brems", "pair", and "3-gluon", again in analogy to QED ideas. The third process, gluons coupling to gluons, has no analogue in QED because photons carry no electric charge, whereas gluons carry color.

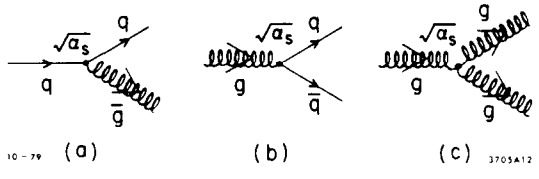

Fig. 8. Basic QCD couplings: a) bremsstrahlung of a gluon from a quark b) pair production of quarks from a gluon, and c) three gluon vertices.

In QED the effective coupling constant varies with Q^2 due to vertex corrections of the electromagnetic current;

$$\alpha(Q^2) = \alpha(Q_0^2)\left[1 - \frac{\alpha(Q^2)}{3\pi}\ \ln\left(\frac{Q^2}{Q_0^2}\right)\right]^{-1} \tag{29}$$

where Q_0^2 is some reference four momentum squared. The strength of the electromagnetic coupling increases as Q^2 increases.

The intuitive explanation has the photon probing shorter distances, allowing the photon to see more of the bare charge, as Q^2 increases. In QCD, the analogous form for α_s is

$$\alpha_s(Q^2) = \alpha_s(Q_0^2)\left[1 + B\alpha_s(Q_0^2)\ \ln\left(\frac{Q^2}{Q_0^2}\right)\right]^{-1} \tag{30}$$

where $B = (33 - 2N_f)/12\pi$ and N_f is the number of quark flavors. Here $\alpha_s(Q^2)$ decreases as Q^2 increases. The intuitive explanation for this behavior is somewhat different. The gluons spread the strong charge out over a finite region of space, so that as Q^2 increases, probing shorter distances, the diffuse strong charge leads to a weakening of the coupling strength. If one introduces the parameter

$$\Lambda^2 = Q_0^2 \exp\left(\frac{-1}{B\alpha_s(Q_0^2)}\right) \tag{31}$$

then

$$\alpha_s(Q^2) = \frac{1}{B}\ \ln\left(\frac{Q^2}{\Lambda^2}\right) \quad . \tag{32}$$

Λ is a free parameter or scale parameter not set by the theory, but which can be determined by experiment. Present values of Λ vary from .1 to 1 GeV, depending on which data samples are used and certain assumptions made in the analyses. The most recent analyses of high Q^2 data show a preference for lower values of Λ. For the values $\Lambda = .5$ GeV and $B = .63$ ($N_f = 4$) Fig. 9 shows the variation of α_s with Q^2. The important feature is the asymptotic approach to 0 as Q^2 increases. The vanishing of the coupling constant at infinite Q^2 represents decoupling of strongly interacting particles in this

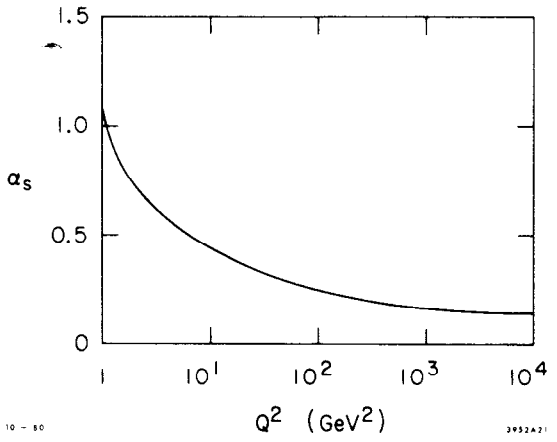

Fig. 9. Variation of α_s with Q^2

limit, and goes by the descriptive phrase "asymptotic freedom".

The prediction of gluons and their coupling to quarks leads to the prediction of scale-breaking in deep inelastic phenomena. Radiation of gluons from quarks leads to an x-distribution that should change as Q^2 increases. Figure 10 shows basic diagram by which scale-breaking should occur. The lepton scatters off constituent quarks, whose distributions are measureable, but not yet calculated in QCD. As Q^2 changes, the process shown in Fig. 9 leads to a

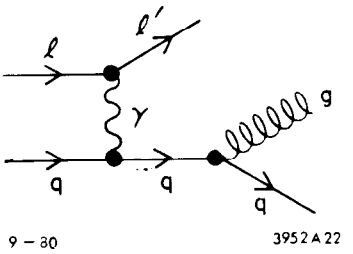

Fig. 10. Gluon radiation from quarks in lepton-nucleon scattering.

change in the quark distributions due to a changing contribution from radiated gluons. At high x, the radiation of gluons should deplete the quark probability distributions. Thus as Q^2 increases the high x part of $F_2(x)$ would be expected to decrease. The pair-production diagram of Fig. 8 allows gluons to contribute to the quark probability at low x. Thus at low x, as Q^2 increases $F_2(x)$ would be expected to increase. The basic QCD-like scale-breaking features of inelastic structure functions is shown in Fig. 11. There are several important, qualitative features which should be emphasized. First, QCD does not predict (yet, at least) the basic shape of the structure functions. As we shall see later, these forms are derived phenomenologically from the data. The variations of the structure functions are predicted in QCD. These variations are not dramatic, but vary logarithmically with Q^2 due to the logarithmic dependence of α_s. The slope of the Q^2 dependence should

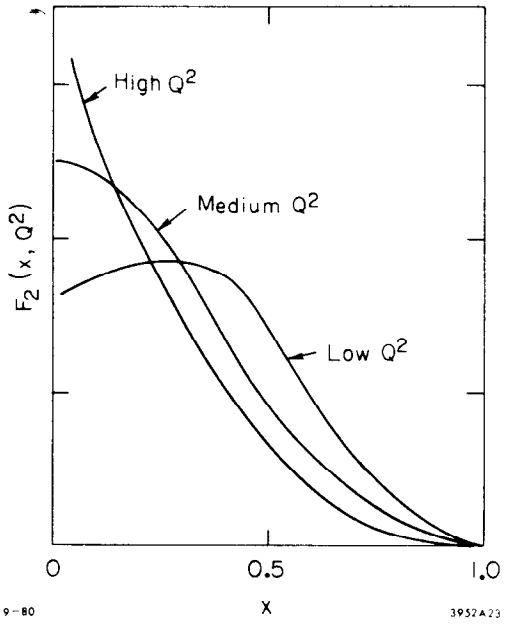

Fig. 11. The qualitative behavior of $F_2(x,Q^2)$ for different values of Q^2 as expected from gluon radiation.

be positive at low x and negative at high x. At present the experimental data are insensitive to the basic gauge group, color SU(3), or the number of quark flavors. The scale-breaking features are sensitive to the spin of the gluon, and later comparison of predictions for vector and scalar gluons will be shown. Finally, one should observe that for a changing distribution as seen in Fig. 11, it is natural to consider moments of the distributions and study their Q^2 dependence. We will next look at QCD predictions of the Q^2-evolution of the structure functions, and then the highly successful and highly controversial moment analysis of the inelastic structure functions.

IV. THE Q^2 EVOLUTION OF THE STRUCTURE FUNCTIONS

It is first necessary to connect the ideas of the quark-parton model to those of QCD. The terminology used in QCD calculations is somewhat different from that already described. For example, it is natural to split off the quark-antiquark pairs that arise in the sea contribution to the structure functions. These components of the structure functions are the so called "flavor singlet" contributions. Gluons coupling to $q\bar{q}$ pairs contribute to flavor singlet structure functions. Unpaired quarks contribute to "flavor nonsinglet" distributions. Quarks radiating gluons (i.e., gluon bremsstrahlung) modify singlet and nonsinglet distributions. Valence quarks contribute to the nonsinglet structure functions. Figure 12 shows the basic terms

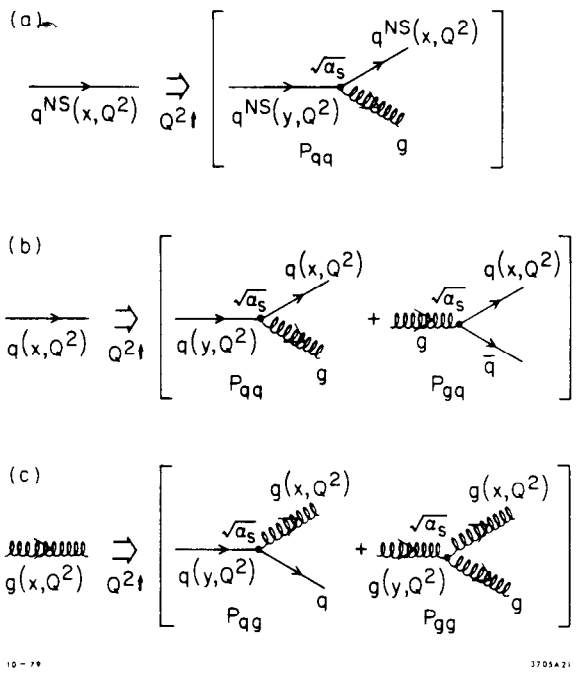

Fig. 12. QCD processes which modify quark distributions: a) flavor nonsinglet (valence) quarks, b) flavor singlet (sea) quarks, c) gluons.

which contribute to the singlet and nonsinglet quark probability distributions.

The singlet and nonsinglet quark distributions are not predicted in QCD. But the quark distributions have a Q^2-dependence modified by terms that appear in Fig. 12. Consider for example the nonsinglet distributions. At low Q^2, the distance scale being probed is relatively long. Emission and reabsorption of quark-antiquark virtual pairs is hidden. But as Q^2 increases, the scale shrinks and quarks are sometimes resolved into a quark of lower momentum and a gluon. The so-called Alterelli-Parisi equation[7] describing this situation is

$$Q^2 \frac{d}{dQ^2} F_2^{NS}(x,Q^2) = \frac{\alpha_s(Q^2)}{2\pi} \int_x^1 \frac{dw}{w} F_2^{NS}(w,Q^2) P_{qq}\left(\frac{x}{w}\right) \tag{33}$$

The fractional change in $F_2(x,Q^2)$ is given by an integral over quark states of higher momenta, times a "splitting function" P_{qq}. The splitting function is a factor representing the emission of a gluon from a quark of momentum w, giving a quark of momentum x. The form of $P_{qq}(z)$ for spin-1 particles is[7]

$$P_{qq}(z) = \frac{4}{3}\left[\frac{1+z^2}{(1-z)_+} + \frac{3}{2}\delta(z-1)\right] \tag{34}$$

where $(1-z)_+$ is defined by the relation

$$\int_0^1 \frac{f(z)\,dz}{(1+z)_+} = \int_0^1 \frac{f(z)-f(1)}{(1-z)}\,dz \quad . \tag{35}$$

We note that

$$\int_0^1 P_{qq}(z)\,dz = 0 \tag{36}$$

and thus $P_{qq}(z)$ is not a probability distribution. The flavor singlet evolution equations are more complicated because of the additional terms which contribute, as illustrated in Fig. 12. For completeness they are included here, but are not used in what follows. One has to introduce a gluon probability distribution $G(x,Q^2)$, and the flavor singlet evolution equations are

$$Q^2 \frac{d}{dQ^2} F_2^S(x,Q^2) = \frac{\alpha_s(Q^2)}{2\pi}\int_x^1 \frac{dw}{w}\left[F_2^S(w,Q^2)P_{qq}\left(\frac{x}{w}\right) + G(w,Q^2)P_{gq}\left(\frac{x}{w}\right)\right] \tag{37}$$

and

$$Q^2 \frac{d}{dQ^2} G(x,Q^2) = \frac{\alpha_s(Q^2)}{2\pi}\int_x^1 \frac{dw}{w}\left[G(w,Q^2)P_{gg}\left(\frac{x}{w}\right) + F_2^S(w,Q^2)P_{qg}\left(\frac{x}{w}\right)\right] \quad . \tag{38}$$

The singlet distributions require one to solve coupled integrodifferential equations. The four splitting functions are predicted in QCD, but the gluons and singlet quark distribution must be obtained from data. The added complexity of the singlet distributions makes them less practical to use.

The singlet and nonsinglet structure functions can be related directly to experimental ones, and thus are readily obtained from

the data;

$$F_2^{ep} = \frac{5}{18} F_2^S + \frac{3}{18} F_2^{NS}$$

$$F_2^{ed} = \frac{5}{9} F_2^S \qquad (39)$$

$$F_2^{ep} - F_2^{en} = \frac{1}{3} F_2^{NS} \quad .$$

The structure function $xF_3^{\nu N}$ is also a nonsinglet distribution. Fig. 13 shows the SLAC/MIT and SLAC data analyzed in terms of singlet and nonsinglet contributions.[8]

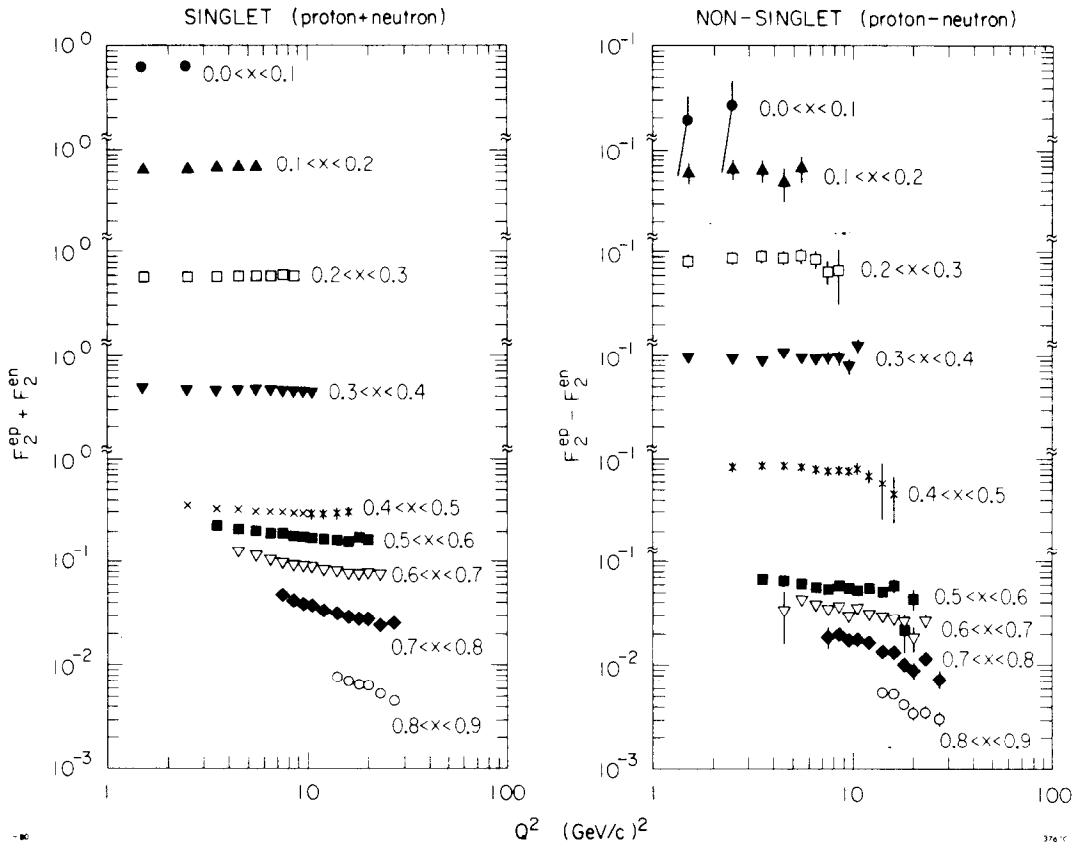

Fig. 13. Singlet and nonsinglet structure functions for eN inelastic scattering (SLAC/MIT and SLAC).

The Alterelli-Parisi evolution equations provide the basis for the phenomenological description of the inelastic structure

functions. An approximate solution to the QCD equations was proposed by Buras and Gaemers in 1978.[9] They proposed analytic expressions of the form

$$xF^{NS}(x,Q^2) = \frac{3}{B(\eta_1(s), 1+\eta_2(s))} x^{\eta_1(s)} (1-x)^{\eta_2(s)} \tag{40}$$

$$xF^{S}(x,Q^2) = A_s(s)(1-x)^{\eta_s(s)} \tag{41}$$

$$xG(x,Q^2) = A_G(s)(1-x)^{\eta_G(s)} \tag{42}$$

where $s \equiv \ell n\,[(\ell n\, Q^2/\Lambda^2) / (\ell n\, Q_0^2/\Lambda^2)]$. The function $B[\eta_1(s), 1+\eta_2(s)]$ is the Euler beta function, required to satisfy the sum rule

$$\int_0^1 xF^{NS}(x,Q^2)\, dx = 3 \quad . \tag{43}$$

The parameterizations, Equations (40-42), are similar to ones used earlier in simple parton model descriptions of the data. Based on SLAC-MIT data and a choice of $Q_0^2 = 1.8$ GeV^2, the parameters η_1 and η_2 have the values

$$\eta_1(s) = 0.70 - 0.176\ s \tag{44}$$

$$\eta_2(s) = 2.60 + 0.8\ s \tag{45}$$

Figure 14 shows $xF_3(x,Q^2)$ in bins of x plotted against the parameter Q^2. The data come from inelastic $\nu,\bar{\nu}$ scattering of the CERN-Dortmund-Heidelberg-Saclay collaboration at CERN.[10] In such a figure, one looks for slopes different from zero as an indication of the degree of scale breaking. In these data, the small x bins show little Q^2 dependence, but at large x, the xF_3 structure function decreases noticeably as Q^2 increases. The solid lines represent the Buras and Gaemers fit to the data. The data clearly show the QCD-like behavior predicted by the Buras and Gaemers analysis.

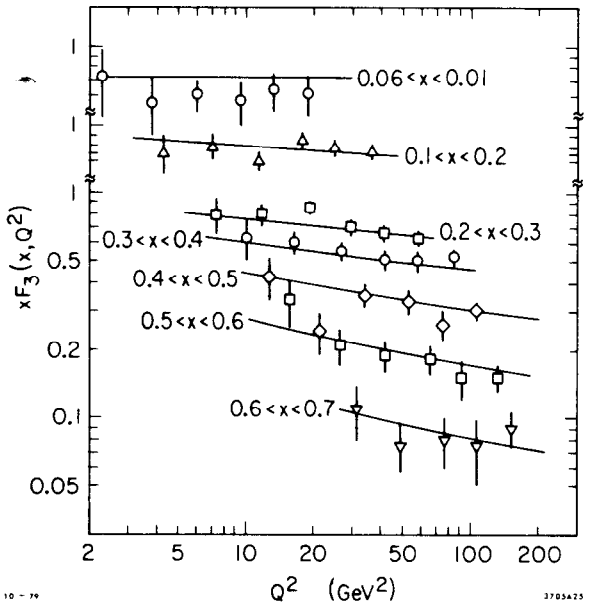

Fig. 14. Method of Buras and Gaemers applied to the neutrino-nucleon structure function xF_3. Solid lines give the result of the last fit to the data (from Ref. 10).

Using the relation equation, (22), the results of Fig. 14 can be extended to lower Q^2 and compared to SLAC eD inelastic data. Figure 15 shows F_2 calculated from the CDHS $F_2^{\nu N}$ results, and the SLAC F_2^{eD} data. The solid

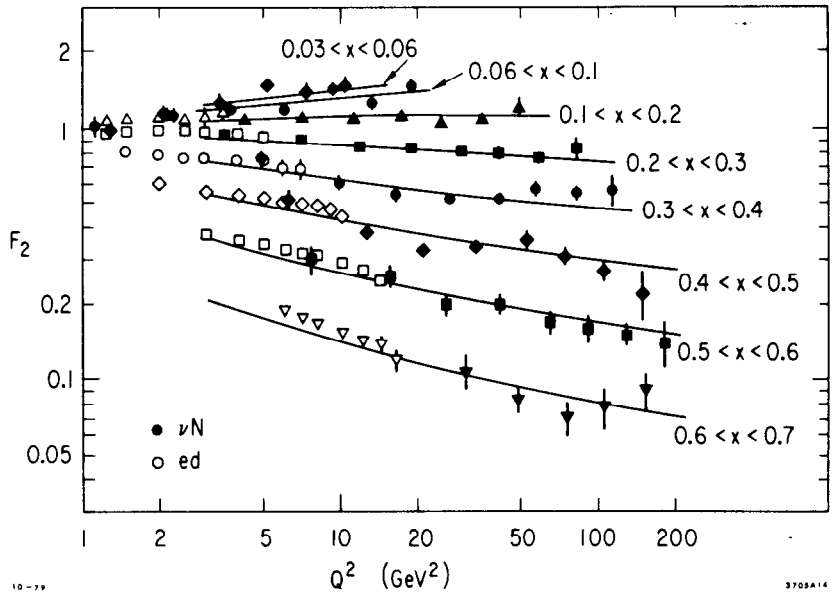

Fig. 15. Structure function F_2 derived from νN (Ref. 10) and ed (SLAC/MIT and SLAC) data. The solid curve is a Buras and Gaemers fit.

curves are Buras and Gaemers results extended to lower Q^2. A noticeable rise in F_2 at low x, and a fall in F_2 at large x, are seen as Q^2 increases.

The degree of scale breaking in these data is measured by the slope of the fits in Figs. 14 and 15. One can define a slope parameter b by

$$\ell n\ F_2 = b\ \ell n\ Q^2 + \text{constant} \tag{46}$$

or more precisely

$$b = \frac{d\left(\ell n\ F_2\right)}{d\left(\ell n\ Q^2\right)} \quad . \tag{47}$$

In Fig. 16 scaling, which corresponds to $b = 0$, is seen to occur for

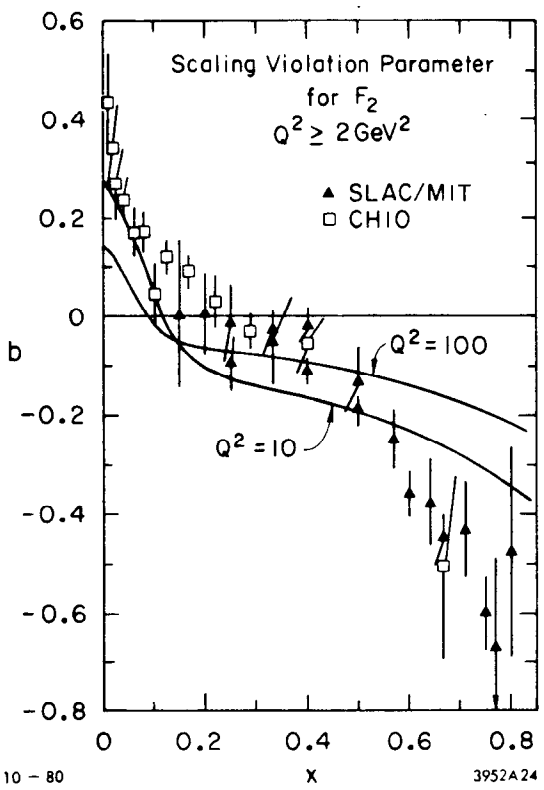

Fig. 16. The scaling violation parameter b for the proton structure function F_2 as a function of x. (From SLAC/MIT and SLAC and CHIO, Ref. 11). The curves are from a Buras and Gaemers parametrization.

a narrow range near x = .2, but is broken significantly for smaller x and for larger x. Curves for b versus x, calculated from the Buras and Gaemers fits are shown for $Q^2 = 10$ GeV^2 and $Q^2 = 100$ GeV^2 to show the QCD predictions for scale-breaking. These curves are not fits to the data in Fig. 16, but come from fits to other data.

The conclusions we find from the data on inelastic structure function and from the Buras and Gaemers analysis are that leading-order QCD provides a good description of eN, μN and νN inelastic scattering, and that scale breaking predicted by QCD is seen in the data.

A more recent analysis of inelastic eN data from SLAC/MIT and SLAC includes effects of the so called "higher twist" terms. Higher twist operators from the operator product expansion formalism contribute power-law terms to leading-order QCD. Abbott, Atwood and Barnett[8] argue that the combination of power-law and logarithmic Q^2 dependences can introduce significant uncertainties into the determination of the scale parameter Λ, resulting in lower values than those obtained from logarithmic Q^2 terms only. They argue that we do not yet know how much scale violation arises from the logarithmic variation of the coupling constant, and how much arises from the higher twist terms, and therefore the conclusions about the success of QCD predictions may be premature.

Abbott, Atwood and Barnett select the SLAC/MIT ep and eD data to obtain singlet and nonsinglet structure functions. They choose a form

$$F_2^S = C_1 x^{C_2}(1-x)^{C_3} \tag{48}$$

$$F_2^{NS} = C_4\left(1 + C_5 x\right)(1-x)^{C_6} \tag{49}$$

$$G = A(1-x)^5 \tag{50}$$

at a value $Q_0^2 = 30$ GeV^2. The choice of Q_0^2 is not particularly significant to the fits. The evolution equations connect these

functions to data at all x and Q^2, but the functional forms for $Q^2 \neq Q_0^2$ will differ from those of Eqs. (48-50).

The best fit parameters are $C_1 = .59$, $C_2 = .85$, $C_3 = 2.7$, $C_4 = 1.9$, $C_5 = 1.0$ and $C_6 = 3.1$. The value for the scale parameter Λ is .63 GeV. Figure 17 shows fits to F_2^{ep} at small W. This figure is interesting in that the behavior of the Bjorken scaling variable x (solid curve) and the Nachtmann scaling variable ξ (dashed curve) are compared at low W. The Nachtmann variable appears to average better the oscillations in F_2 due to nucleon resonances at low Q^2. Notice also that the elastic peak contribution is large at low Q^2. Abbott, Atwood and Barnett cut their data at $Q^2 \geq 4$ GeV^2 due to uncertainties in

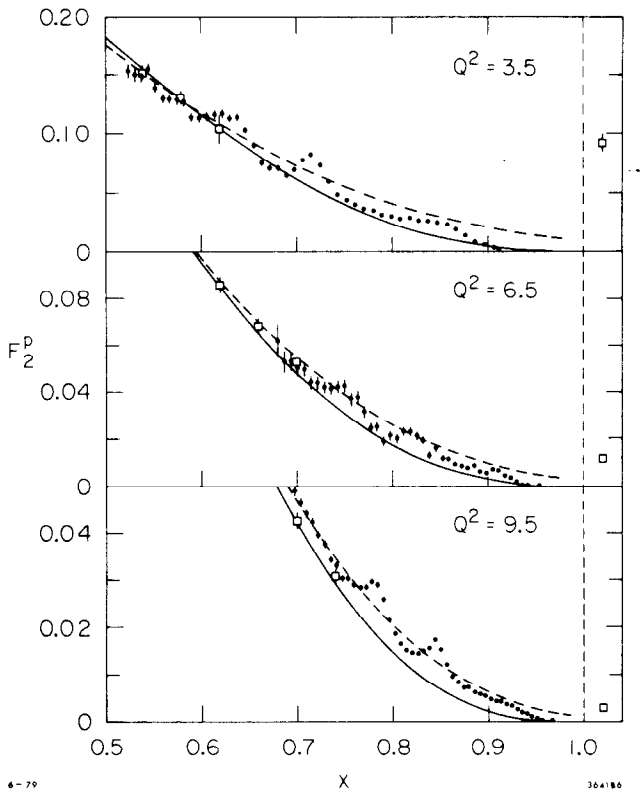

Fig. 17. The structure function F_2 for eN scattering in the region of low W. The structure due to nucleon resonance is better averaged by the use of the variable ξ (dashed curve) than x (solid curve). The elastic peak cross section is shown in the bin above x = 1.

the interpretation of the very low Q^2 data. They conclude that the SLAC data for $F_2(x,Q^2)$ are entirely consistent with predictions of QCD, but uncertainties from higher twist terms prevent determination of the scale parameter Λ within a factor of two, and may even prevent one from observing the logarithmic nature of scale breaking. At the time of their analysis, no high Q^2 data of sufficient precision to improve the fits was available to them. As we shall see later, recent experiments of good quality are now producing new data which may resolve the issue of power-law versus logarithmic Q^2-dependence in the structure functions.

V. MOMENTS OF THE STRUCTURE FUNCTIONS AND TESTS OF QCD

The QCD prediction of scale-breaking in inelastic structure functions leads to a qualitative picture shown in Fig. 11. As Q^2 increases, the structure functions shift to lower values of x. The mean and all higher moments should decrease as Q^2 increases. It has been shown in QCD that the moments have relatively simple functional forms, and studies of the Q^2 dependence of the moments has been quite popular.

Define the nth moment of a nonsinglet structure function to be

$$M_i^{NS}(n,Q^2) = \int_0^1 x^{n-2} F_i^{NS}(x,Q^2)\, dx , \qquad i = 1,2,3 \tag{51}$$

There are two sources of nonsinglet structure functions:

(i) xF_3 from νN inelastic scattering, and

(ii) $F_2^{ep} - F_2^{en}$ from ep and eD data.

In QCD the nonsinglet moments have the particular simple form (in leading-order)

$$M^{NS}(n,Q^2) \sim \ell n \left(\frac{Q^2}{\Lambda^2}\right)^{-d_n} \tag{52}$$

where the d_n are constants called "anomolous dimensions" and for

vector gluons are given by[12]

$$d_n = \frac{4}{25}\left[1 - \frac{2}{n(n+1)} + 4\sum_{j=2}^{n}\frac{1}{j}\right] \tag{53}$$

Values of d_n are given in Table I. We note that d_n is independent of the number of quark flavors and independent of the color gauge group, but does depend on the vector nature of the gluons.

Table I. Values of d_n

n	d_n
2	.43
3	.67
4	.84
5	.97
6	1.08

The constants of proportionality implied in Eq. (52) are eliminated by taking ratios of moments

$$M^{NS}(n,Q^2) = \text{const}\left[M^{NS}(m,Q^2)\right]^{\frac{d_n}{d_m}} \tag{54}$$

or

$$\ell n\, M^{NS}(n,Q^2) = \text{const} + \frac{d_n}{d_m}\,\ell n\, M^{NS}(m,Q^2) \tag{55}$$

Figure 18 shows how such a plot should appear. As Q^2 increases, both nth and mth moments decrease, and the ratio, plotted on log-log graphs should move along a straight line of slope d_n/d_m.

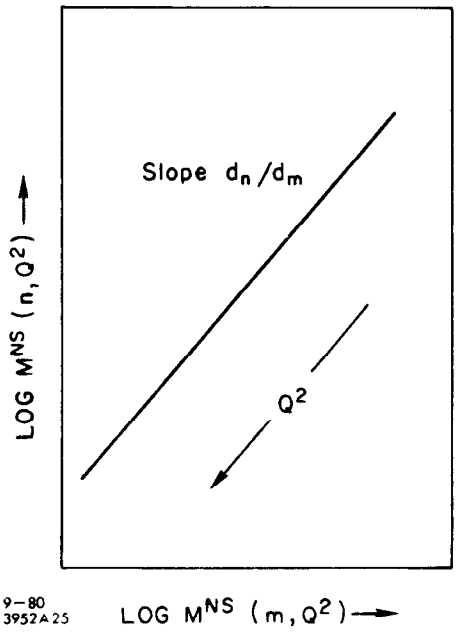

Fig. 18. Expected behavior for mth vs nth moments plotted on log-log scales.

Because of the logarithmic dependence one problem to be encountered is the need for a large range of Q^2 in the data. Therefore, one sees low Q^2 data being included in these moment analyses. Low Q^2 data implies low W cuts on the data, and

the issue of which scaling variable to use arises. Equation (54) defines the so-called Cornwall-Norton moments of F_i^{NS}. We saw earlier that the use of the Nachtmann scaling variable ξ fit better the data at low W. Nachtmann showed that finite target mass effects could be better accounted for by use of the variable ξ, and he redefined the moments to be

$$M_i\left(n,Q^2\right) = \int_0^1 dx \; \frac{\xi^{n+1}}{x^k} \, K_i\left(n,x,Q^2\right) \, F_i\left(x,Q^2\right) \tag{56}$$

where $k = 2$ for $i = 3$, and $k = 3$ for $i = 2$ and

$$K_2\left(n,x,Q^2\right) = \frac{n^2+2n+3+3(n+1)\left(1+\frac{4m^2x^2}{Q^2}\right)^{\frac{1}{2}} + n(n+2)\left(\frac{4m^2x^2}{Q^2}\right)}{(n+2)(n+3)} \tag{57}$$

$$K_3\left(n,x,Q^2\right) = \frac{1+(n+1)\left(1+\frac{4m^2x^2}{Q^2}\right)^{\frac{1}{2}}}{(n+2)} \quad . \tag{58}$$

These moments are called the Nachtmann moments.[13] They are usually preferred because they take into account the finite masses.

Figure 19 shows two ratios of moments, M_6/M_4 and M_5/M_3, for the xF_3 structure function from BEBC-Gargamelle bubble chamber data and the CDHS data from CERN. The solid line shows the prediction for vector gluons, while the dashed line shows the prediction for scalar gluons. The data prefer a vector gluon description and argue against the scalar fit. A slanted axis shows the approximate Q^2 value of the data points. Figure 20 shows the same analysis applied to the SLAC/MIT ep and eD data. The nonsinglet structure function used here is $F_2^{ep} - F_2^{en}$, described earlier. Clearly the vector gluon description is preferred over the scalar one in these data, too. We see in Figs. 19 and 20 a remarkable agreement between QCD predictions and data. This seems to be a dramatic success for leading-order QCD. But a number of objections and problems still cloud this conclusion. First, these moments are sensitive to the choice of scaling variable,

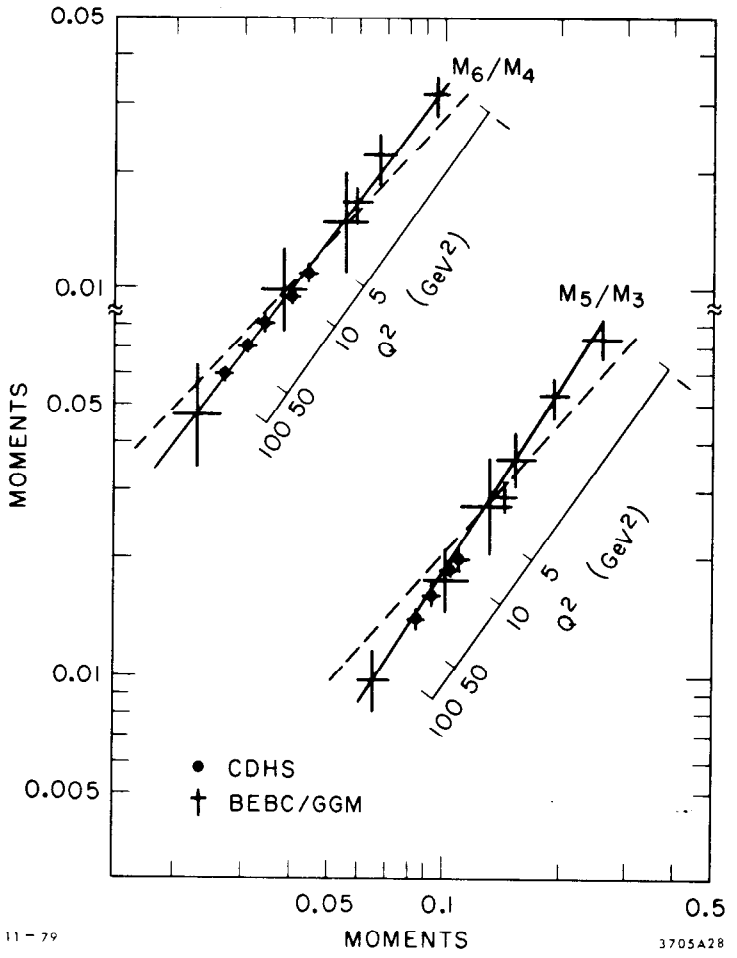

Fig. 19. Moments of xF_3 structure functions from νN scattering plotted against each other. Solid lines show vector gluon predictions; dashed lines are for scalar gluons.

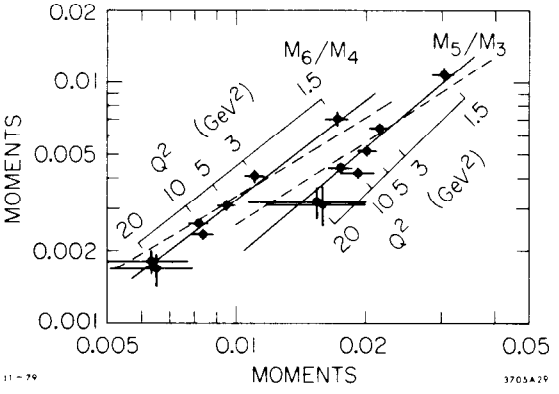

Fig. 20. Moments of nonsinglet structure functions $F_2^{ep} - F_2^{en}$ plotted against each other. Solid lines show vector gluon predictions; dashed lines are for scalar gluons.

and limiting the data to kinematic territory where choice of scaling variables is not important considerably restricts the amount of data available. Second, the moment integrals at low Q^2 includes considerable amount of elastic peak. The higher moments are dominated by the elastic contribution, and the validity of including elastic cross sections in the integrals is an assumption. Figure 21 shows the integrand for F_2^{ep} for three moments, illustrating how the higher moments become sensitive to low W states. Third, because different moments are highly correlated through the use of the same data, errors on Figs. 19 and 20 are completely misleading. In fact the data points seems to prefer to fall on the predicted curve even where known problems, such as normalization errors, exist in the data. There seems to be a puzzling confirmation of QCD predictions independent of the quality of the data. Finally, and perhaps most seriously, there appear to be terms in leading order arising from the higher twist operators which can contribute additional power-law factors. The leading order

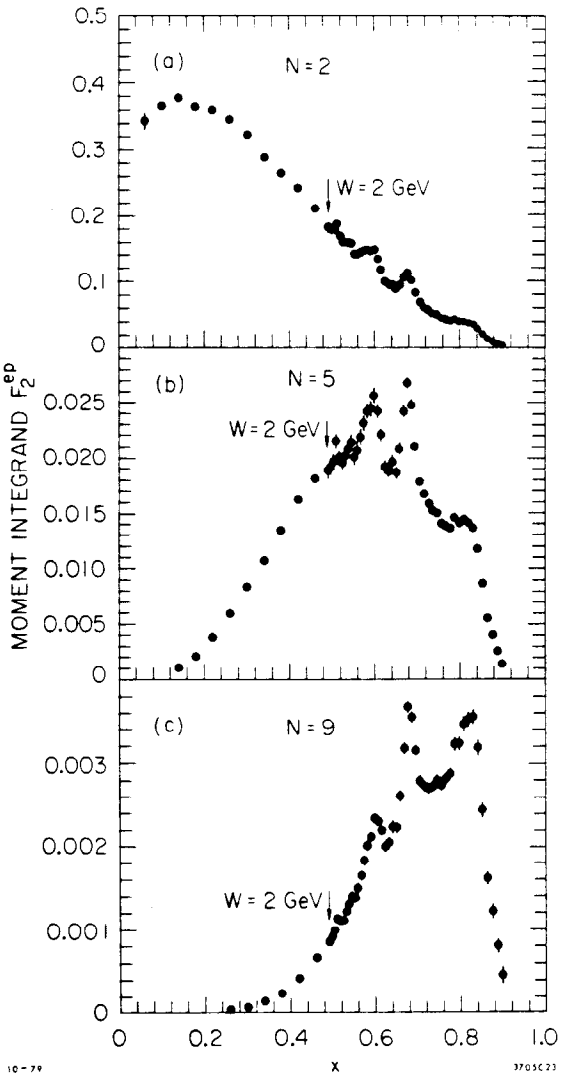

Fig. 21. Integrands for three moments of F_2^{ep}. Note that the high x part of the data is heavily weighted in the higher moments. Low W states dominate the higher moment integrands at low Q^2.

logarithmic Q^2 dependence may, in the final analysis, turn out to be an improper form.

Support for the notion that second order terms are important in inelastic scattering phenomenology comes from the analysis of Duke and Roberts.[14] They take leading order formulations to extract the scale parameter Λ from the different moments of the SLAC/MIT, BEBC and CDHS data. The results for Λ_n versus n are shown in Fig. 22. The most precise data, from $F_2^{ep} - F_2^{en}$ of the SLAC/MIT experiments, show a strong n-variation. The BEBC and CDHS data show much less variation. The interpretation comes from a calculation by Bardeen[15] where Λ_n is calculated in leading order, but with next-to-leading order effects included. The results are shown by the dashed curve. Λ_n is expected to have an n-dependence if higher order terms are present, and the indications from the data can be taken as a possible evidence for higher order effects in the data.

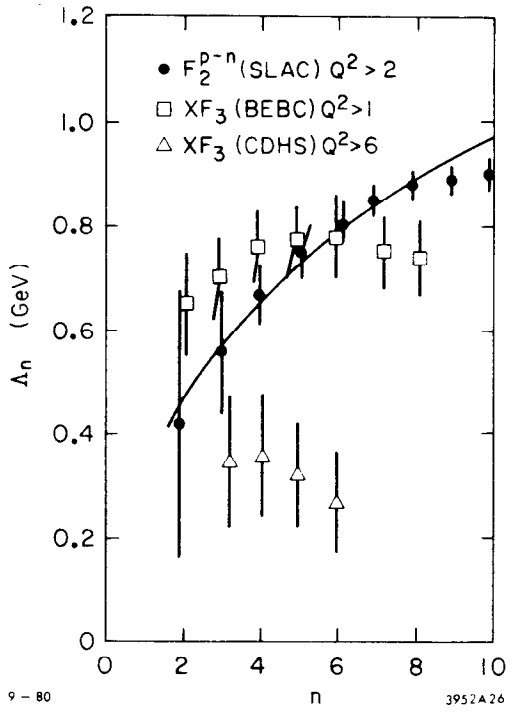

One could summarize the situation by saying that the qualitative features of QCD are seen in the data, and leading order QCD can provide a good description, but at the quantitative level much work remains. In the theory there is the need to understand the effects of higher twist operators and to extend the calculations beyond leading order.

Fig. 22. Experimental Λ values obtained by Duke and Roberts (Ref. 14) using BEBC, CDHS and SLAC/MIT and SLAC data. The solid curve is a calculation which includes second-order effects (Refs. 12 and 15).

In the experiments we need high quality data that extends the kinematic range to the very high Q^2 values now possible.

VI. THE PARAMETER R

No review of deep inelastic phonomena is complete with a discussing of the parameter R. Let me begin with a definition of this important parameter. Electrons (and muons) can radiate real and virtual photons. In the case of real photons, there are only two spin states which contribute, $J_z = \pm 1$ where z refers to the direction of photon propagation. It is well known that real photons are transversely polarized, and the resulting cross section is denoted σ_T (T for transverse). For virtual photons, an additional component can also contribute, $J_z = 0$. The cross sections resulting from the $J_z = 0$ component of the electromagnetic current is denoted σ_L (L for longitudinal). When one sums over all hadronic final states (i.e., inclusive electroproduction) there are no interference terms present. The cross section previously expressed in terms of the structure functions F_1 and F_2 in Eq. 12, has the form

$$\frac{d^2\sigma}{dQ^2 dx} = \Gamma\left(\sigma_T + \varepsilon\sigma_L\right) \quad . \tag{59}$$

The factors Γ and ε are readily calculated in the single-photon-exchange approximation and are referred to by the names "flux factor" and "polarization parameter", respectively.

The parameter R is defined to be

$$R = \sigma_L / \sigma_T \tag{60}$$

which is a function of the kinematic variables, for example x and Q^2. Experimentally one obtains R by measuring cross sections at fixed x and Q^2, but at different values of ε. One can vary the incident beam energy E_0 and the lab scattering angle θ such that x and Q^2 are held fixed, but resulting in different ε values. In practice experiments

cover a grid of values of E_0 and θ, and after radiative corrections have been applied, data are interpolated to chosen values of x and Q^2. One than plots $(1/\Gamma)(d^2\sigma/dQ^2dx)$ versus ε for each chosen value of x and Q^2. The resulting data points, illustrated in Fig. 23, should fall on a straight line whose intercept at $\varepsilon = 0$ is σ_T and whose slope is R.

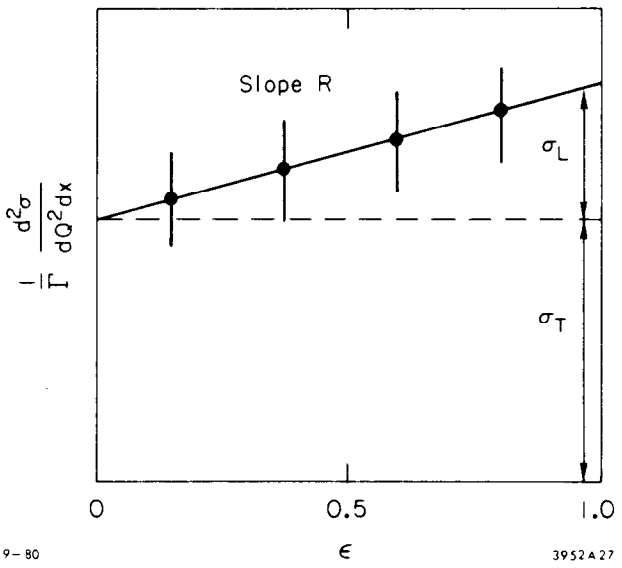

Fig. 23. Expected eN cross section dependence on the parameter ε.

In terms of the kinematic parameters

$$\Gamma = \frac{\alpha}{\pi} \frac{MKy^2}{Q^4(1-\varepsilon)} \tag{61}$$

and

$$\varepsilon = \frac{1}{\left[1+2\tan^2\left(\frac{\theta}{2}\right)\left(1+\frac{\nu^2}{Q^2}\right)\right]} \tag{62}$$

where

$$K = \frac{W^2 - M^2}{2M} \tag{63}$$

The previously defined structure functions are

$$F_1(x,Q^2) = \frac{MK}{4\pi^2\alpha}\sigma_T(x,Q^2) \tag{64}$$

and

$$F_2(x,Q^2) = \frac{\nu K}{4\pi^2\alpha}\left(\frac{Q^2}{Q^2+\nu^2}\right)\left[\sigma_T(x,Q^2) + \sigma_L(x,Q^2)\right] \tag{65}$$

In terms of these more familiar structure functions

$$R = \frac{\sigma_L}{\sigma_T} = \frac{F_2(x,Q^2)}{2xF_1(x,Q^2)}\left(1+\frac{Q^2}{\nu^2}\right) - 1 \tag{66}$$

Recall now the Callan-Gross relation $2xF_1 = F_2$. In the Bjorken limit $\nu^2 >> Q^2$, R = 0 implies Callan-Gross. But at finite energies,

exact Callan-Gross is not consistent with R = 0, but with a small value given by

$$R_c = \frac{Q^2}{\nu^2} = \frac{4M^2x^2}{Q^2} \tag{67}$$

We learn from this relation that at finite energies, finite mass targets lead to nonzero values of R.

Why is R an interesting parameter? It is sensitive to the spin of the constituents. In Fig. 24 we see a current scattering off a constituent particle in the Breit Frame. Helicity is conserved for massless particles, due to the vector nature of the coupling for electromagnetic processes

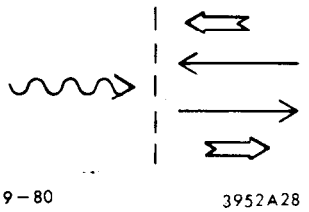

Fig. 24. Electromagnetic or weak current scattering off a spin-½ constituent preserves helicity; the J_z=0 contribution (σ_L) should vanish, giving R = 0.

(and for vector and axial-vector couplings of the weak currents). Spin flip occurs for spin one constituents, corresponding to $J_z = \pm 1$ components of the current only. $R = \sigma_L/\sigma_T = 0$ in this limit. On the other hand, for spin-0 constituents, $J_z = 0$ components contribute, and R = infinity. For a mixture of spins, R will fall in between. Since we do not work in the Bjorken limit, or with massless particles, contributions to R come from

(i) Finite mass constituents: $R \simeq 4m^2x^2/Q^2$

(ii) Transverse momenta giving spin flip terms: $R \cong \langle P_t^2 \rangle / Q^2$

(iii) QCD effects such as transverse momenta from gluon emission: $R \sim \alpha_s Q^2/\nu^2 = \alpha_s 4M^2x^2/Q^2$

(iv) "Diquark" constituents (coherent scattering off quark-pair bosons): R rises at large x.

The difficulty with interpreting data in R, and particularly with

confronting QCD predictions for R, is that no theory effectively combines these processes in a comprehensive way.

Figure 24 shows the SLAC/MIT and SLAC inelastic scattering experiments in a highly schematic form. The detector is moveable and can be set at various laboratory angles θ. The beam energy can be varied up to approximately 25 GeV. From the grid of data points obtained one interpolates to common bins of x and Q^2 for various values of the polarization parameter ε. The errors in these procedures are dominated by systematic uncertainties arising from spectrometer solid angle, for example, and from uncertainties in the radiative correction procedures. Systematic errors have been added in quadrature with the statistical errors. An example of one R measurement is shown in Fig. 25, where the data are all taken at $W^2 = 7$ GeV^2 and $Q^2 = 9$ GeV^2. The approximate laboratory angle for these data are shown at the top of the graph. The values of ε are shown on the horizontal axis. Note the suppressed zero on the vertical axis. The best straight line fit is shown, corresponding to R = .21. A dashed curve shows the straight line fit that would result if radiative corrections were not applied.

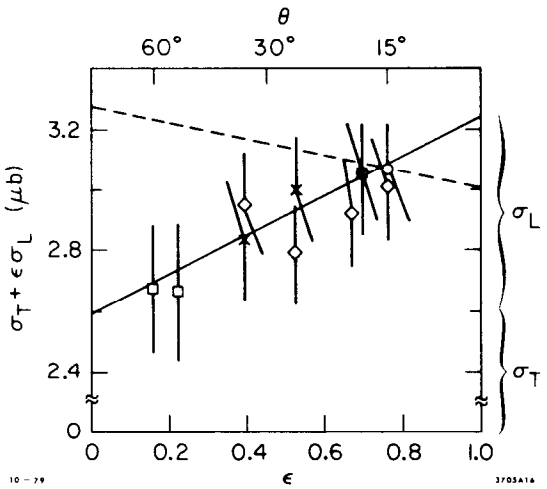

Fig. 25. Cross sections versus ε for ep scattering. $Q^2 \approx 9$ GeV^2 and $W^2 \approx 7$ GeV^2. The solid curve is a fit for R = .21; the dashed curve results from using data not corrected for radiative processes, and illustrates the sensitivity of R to experimental corrections.

The procedures leading to data like those shown in Fig. 24 are referred to as "separations" of the structure functions. In principle only separation of the data can lead to experimental determination of F_1 and F_2. Most experiments do not have enough data of high

quality to make these separations, and it is a common practice to make a simplifying assumption such as the Callan-Gross relation, or an assumed value of R.

The SLAC/MIT and SLAC data represent the most extensive separations taken up to the present. Figure 26 shows the data for $ep \to eX$ for the entire range of W^2 and Q^2 where separations have occurred. The previous figure is included in this one. It is possible to fit these data with a single, constant value for R. The best value is

$$R_p = .21 \pm .10 \text{ (hydrogen data)} \tag{68}$$

Figure 27 shows the same data for the reaction $eD \to eX$. The data are very similar to that seen for hydrogen targets, with a best constant

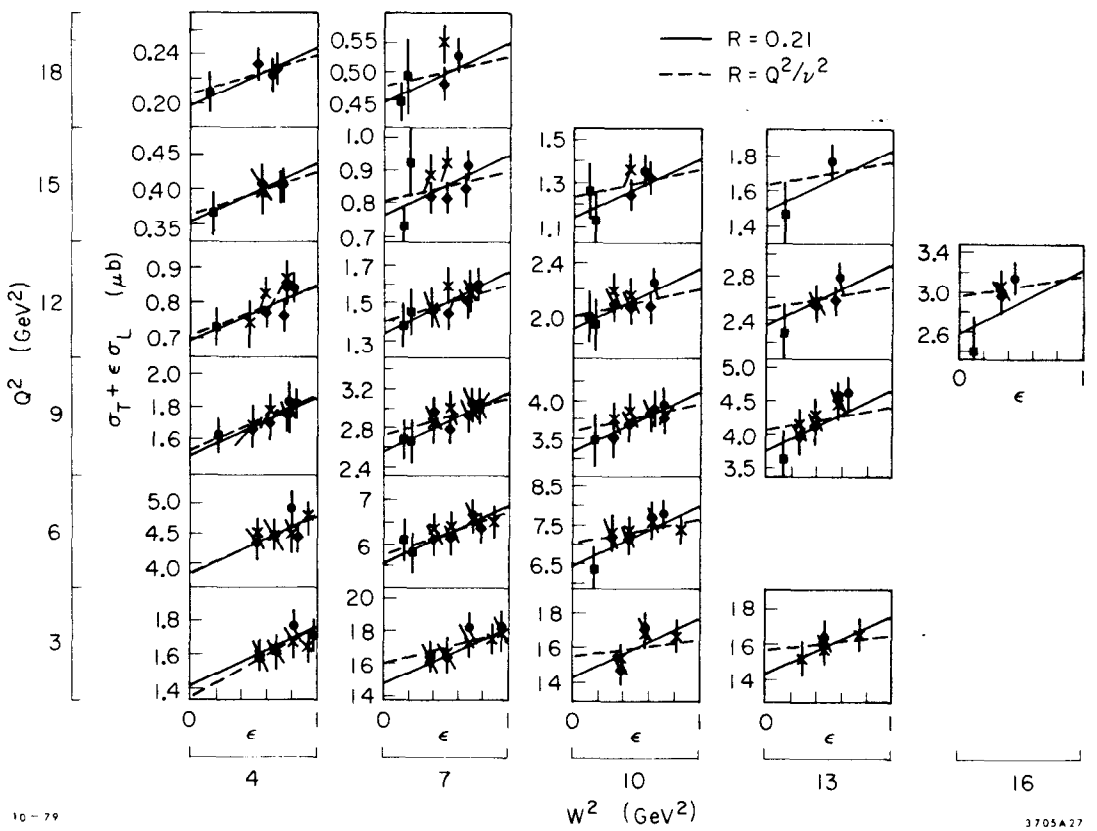

Fig. 26. ε plots for the Q^2, W^2 range of SLAC ep data.

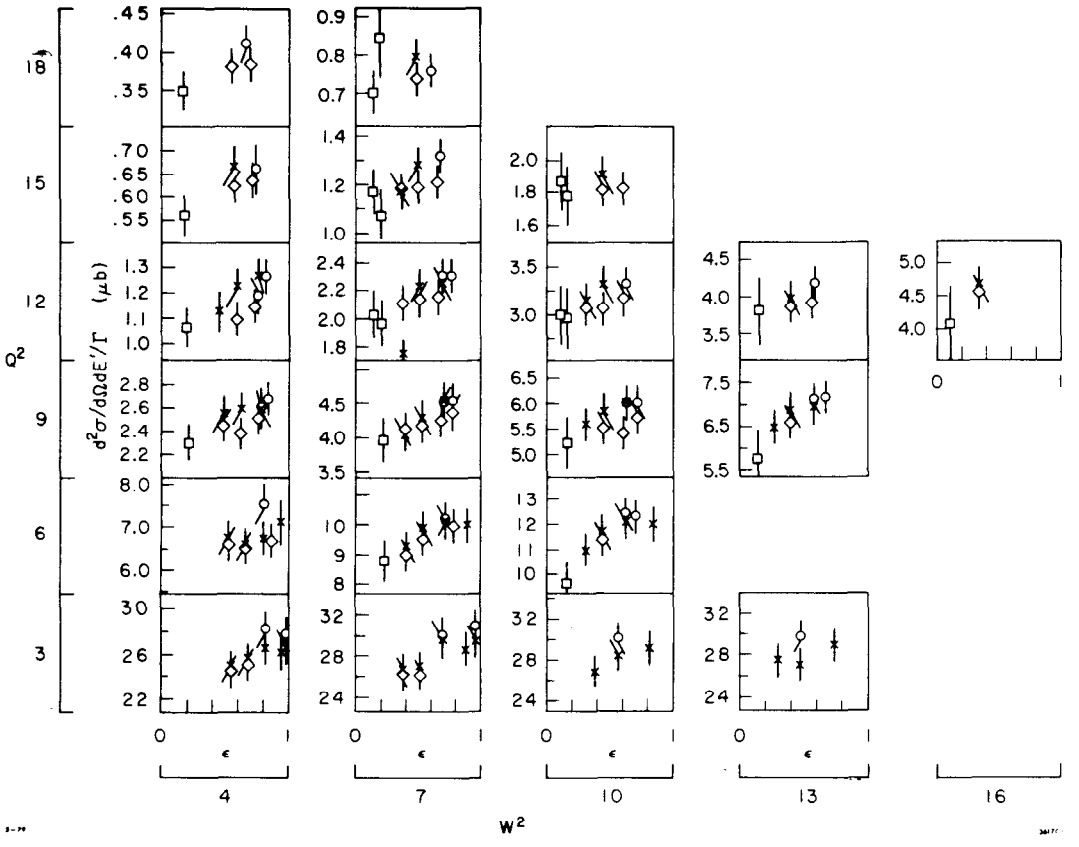

Fig. 27. ε plots for the Q^2,W^2 range of SLAC ed data.

value

$$R_d = .24 \pm .10 \quad \text{(deuterium data)} \tag{69}$$

In inelastic neutrino scattering it has been customary to define a different, but closely related, R parameter. It is

$$R_\nu = 1 - \frac{2xF_1}{F_2} \tag{70}$$

which represents the deviation of cross section results from exact Callan-Gross. Using Eq. (66), one finds the relationship to the electroproduction R to be

$$R_\nu = \frac{R - \frac{Q^2}{\nu^2}}{R+1} \tag{71}$$

R_ν can be measured in νN and $\bar{\nu}N$ inelastic scattering by looking at the y dependence of the cross section given by

$$\left(\frac{d\sigma^\nu}{dy} + \frac{d\sigma^{\bar{\nu}}}{dy}\right) = \frac{G^2 M E_0}{\pi} F_2 \left[1 + (1-y)^2 - y^2 R_\nu\right] \tag{72}$$

where data have been accumulated over a range of x values. The data are fit to the form, Eq. 72, with R_ν a free parameter of the fit. Figure 28 shows the results from the CDHS collaboration at CERN.[16]

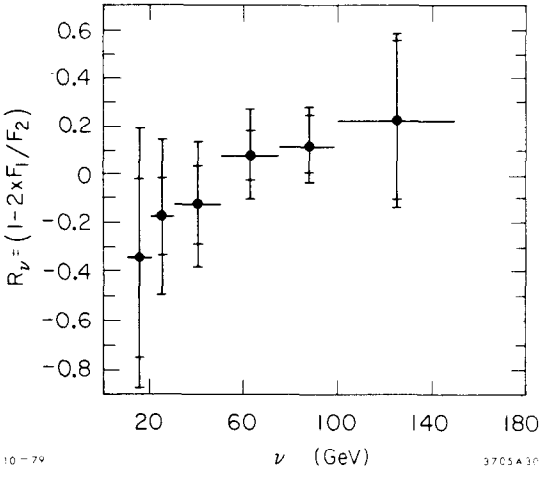

Fig. 28. R_ν, the deviation from the Callan-Gross relation, versus ν.

Their results, plotted against the energy transferred to the hadrons, ν, show that within errors, the neutrino data are consistent with the Callan-Gross relation. Another neutrino experiment, the BEBC bubble chamber at CERN, report a value of $R = .15 \pm .10$ (stat. error) $\pm .04$ (sys. error), obtained by fitting y distributions for fixed bins of x and Q^2.[17]

Figure 29 summarizes these results for R. Three experiments, SLAC/MIT and SLAC, Chicago-Harvard-Illinois-Oxford, and BEBC, are included in the figure. The CDHS results of Fig. 28 are not shown, but are included in spirit by showing what exact Callan-Gross relations imply for the SLAC data at the mean Q^2 and x values of the data.

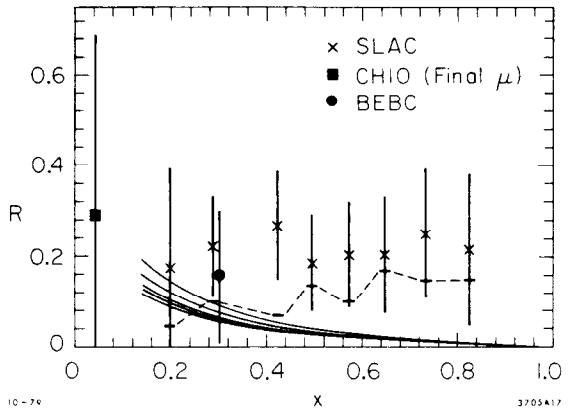

Fig. 29. $R = \sigma_L/\sigma_T$ versus x for BEBC (Ref. 17), CHIO (Ref. 11) and SLAC data. The solid lines are R_{QCD}; the dashed curve is $R = Q^2/\nu^2$ (Callan-Gross) for the $\langle Q^2 \rangle$ of each SLAC data point.

In QCD, the parameter R can pick up contributions from gluon emission at high x, and pair-production of quarks at low x, both of which give quarks transverse momentum. The QCD contribution to R is proportional to the coupling $\alpha_s(Q^2)$ times an integral over $F_2(x,Q^2)$ and $G(x,Q^2)$, the gluon distribution function.[8] An approximate form used by the CHIO collaboration[11] is

$$R_{QCD} = \frac{R_0(1-x)}{\ell n\left(\frac{Q^2}{\Lambda^2}\right)} \quad . \tag{73}$$

Figure 29 shows the QCD predictions as described in Ref. 8, for different values of Q^2 from 3 to 18 GeV^2.

Based on the above discussions and data, one concludes that the parameter R is not a good choice for testing QCD predictions. The experiments are all consistent within errors and the Callan-Gross relation, $2xF_1 = F_2$, is a good approximation to the data. Leading-order QCD predictions fall low compared to the data at high x, and errors on the data are too large to see the predicted rise at small x.

VII. RECENT EXPERIMENTAL RESULTS

It is perhaps appropriate to conclude this review of deep inelastic phenomena with a look at current experiments in the field. Although the lectures have been biased toward somewhat older data, which are well established in the literature, several recent experiments currently running or recently completed have begun to provide us with high quality results at high energies for Q^2 out to 200 GeV^2. These experiments cover hydrogen, deuterium, carbon and iron targets. Table II summarizes experiments which are now contributing data to

Table II. Charged Lepton Inelastic Scattering Experiments

Group(s)	Beam	Target	Laboratory
SLAC/MIT and SLAC (6 experiments)	e^-	H,D	SLAC
CHIO	μ^+	H,D	Fermilab
EMC	μ^+	H,D	CERN (NA_2 area)
EMC	μ^+	Fe	CERN (NA_2 area)
BCDMS	μ^+	C	CERN (NA_4 area)
BFP	μ^+	Fe	Fermilab
MSU-F	μ^+	Fe	Fermilab

charged lepton deep inelastic scattering. A number of inelastic scattering experiments will not be discussed, most notably the νN experiments which are covered in other lectures. Final state studies in the hadrons is an important aspect of inelastic phenomena which will be omitted due to limited time. Some of these experiments also report studies of multimuon production. Those who wish to learn more about this interesting subject are directed to the references. I will give a general description of these experiments and look at data that bear on the question of structure functions and scale-breaking. There will be some intercomparison of experimental data

to allow one to judge the quality of the experiments. The main objective in discussing these recent experiments is to raise the awareness of new results which have been recently published or may soon be coming out.

A. The Chicago-Harvard-Illinois-Oxford Collaboration[11] (CHIO)

This group has recently concluded two experiments at Fermilab in a positive muon beam studying the reaction

$$\mu^+ p \rightarrow \mu^+ X$$

at energies of 96, 147 and 219 GeV. Figure 30 shows a schematic view

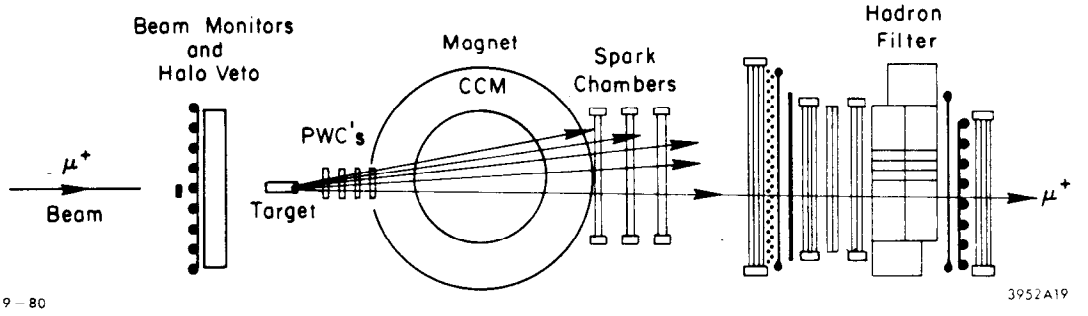

Fig. 30. Schematic layout of CHIO experiment at Fermilab (Ref. 11).

of their experimental apparatus. The detector was based on the rebuilt magnet of the Chicago synchrocyclotron. It produces a field of 1.5 Tesla and has an $\int Bdl$ of 7.5 Tesla-meters. Incident beam particles first encountered a veto wall to eliminate off-axis "halo" muons from the trigger. A liquid hydrogen (or dueterium) target, 120 cm long, was used. Proportional wire chambers before the magnet and magnetostrictive spark chambers behind the magnet determined the angle and momentum of outgoing particles. Crossed scintillator hodoscopes, steel and lead walls followed by chambers permitted triggering, and separation of electrons and photons from hadrons. The scattering muon was identified by hodoscopes and spark chambers placed after the absorbers.

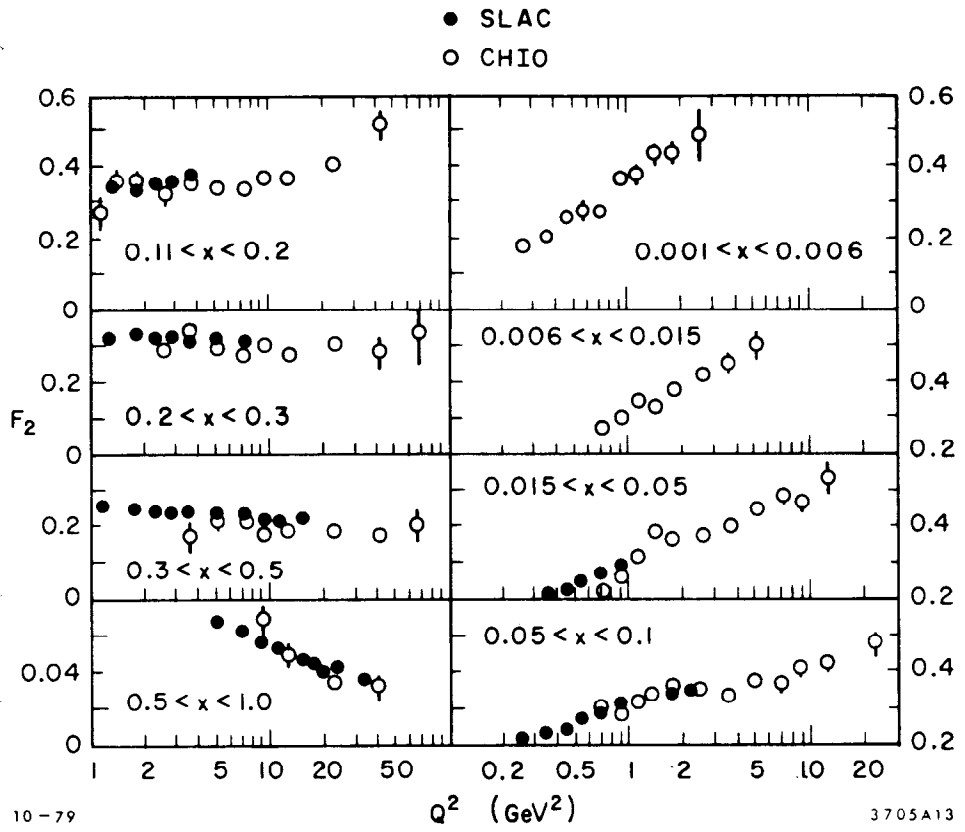

Fig. 31. Comparison of the proton structure function F_2 from ep (SLAC/MIT and SLAC) and μp (CHIO) scattering from $8 \leq Q^2 \leq 10$ GeV^2.

Figure 31 shows the structure function F_2 for eight bins of x. SLAC/MIT data are included to show the consistency between experiments as well as the kinematic regions of the data. Extraction of F_2 required calculations of geometric detection efficiencies, corrections for tracking efficiencies, and background subtractions. Radiative corrections were applied and a value of $R = .52 \pm .35$, consistent with measurements over a subset of the data, was assumed.

Figure 31 shows clear QCD-like scale-breaking features, particularly compared with SLAC data. F_2 increases with Q^2 at low x, and decreases with Q^2 at high x. There is generally good agreement in normalization between the two sets of results. The CHIO data fills

in the low x region of these figures. SLAC data are kinematically excluded from low x at moderate Q^2.

Figure 32 shows better the comparison of SLAC and CHIO data. Here F_2 is plotted as a function of x for the values of Q^2 from 8 to 10 GeV^2. The CHIO data clearly fill in the low x regions not reached by SLAC experiments.

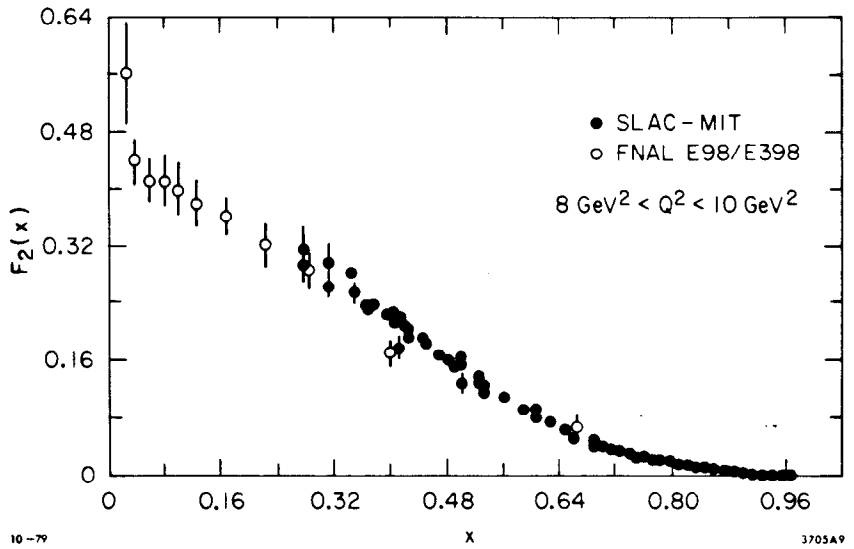

Fig. 32. Comparison of the proton structure function F_2 from ep (SLAC/MIT and SLAC) and μp (CHIO) scattering from $8 \leq Q^2 \leq 10$ GeV^2.

Figure 33 shows R measurements from CHIO for low x. Fits to the forms

$$R = R_0 \frac{1-x}{Q^2}$$

$$R = R_0 \frac{1-x}{\ell n\left(\frac{Q^2}{\Lambda^2}\right)} \quad (\Lambda = .5 \text{ GeV}) \tag{74}$$

and

$$R = R_0$$

for R_0 = 1.20, 1.18 and .52, respectively, are all satisfactory

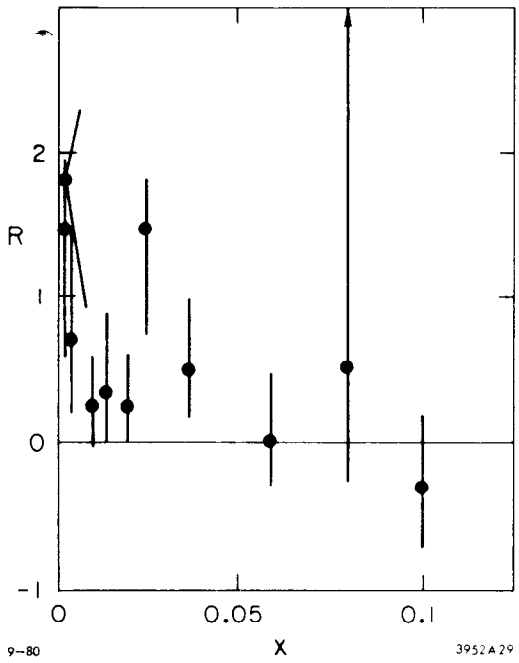

Fig. 33. Measurements of $R = \sigma_L/\sigma_T$ at low x from CHIO (Ref. 11).

within the relatively large errors reported. These errors are too large to establish a rising R at low x as predicted in QCD, but the data are consistent with such behavior.

B. The European Muon Collaboration[18]

Figure 34 shows a schematic layout of a very large and comprehensive experiment presently taking data at CERN in the NA_2 area. They report data from positive muons on hydrogen, deuterium and iron targets at beam energies of 120, 250 and 280 GeV. The experiment is conceptually similar to the one previously discribed. Incident beam muons first encounter a veto wall which eliminates halo muons from the trigger. A six-meter-long liquid hydrogen (or deuterium) target provides the

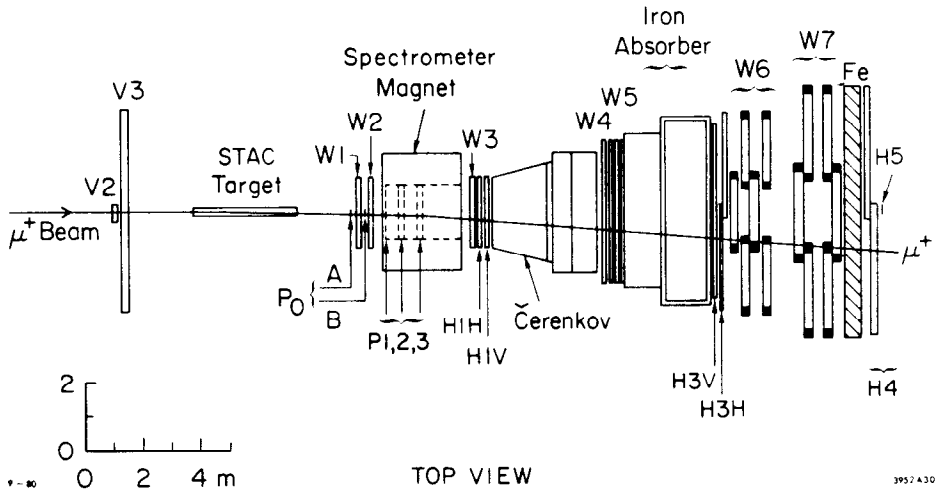

Fig. 34. Schematic layout of EMC experiment at CERN (Ref. 18)

scattering nuclei. The cryogenic target can be replaced with an iron-scintillator sandwich target ("STAC" target for "sampling total absorption counter") used in the measurement of Fe cross sections. Scattered particles are detected in a series of drift chambers upstream and downstream of the forward spectrometer, a wide-gap dipole magnet of $\int Bdl = 5.2$ Tesla-meters. Downstream of the spectrometer are located a hodoscope for fast triggering, proportional chambers for particle tracking, a gas Čerenkov counter to aid in particle identification, and a magnetized iron hadron absorber. Muons are identified and tracked behind the absorber. Structure functions were obtained based on calculations of geometric efficiencies, corrections for multiple scattering effects, tracking inefficiencies, and radiative corrections. To separate F_2 from the data, a value of R = .2 was assumed.

In Fig. 35, the structure function F_2 is shown for fixed x bins

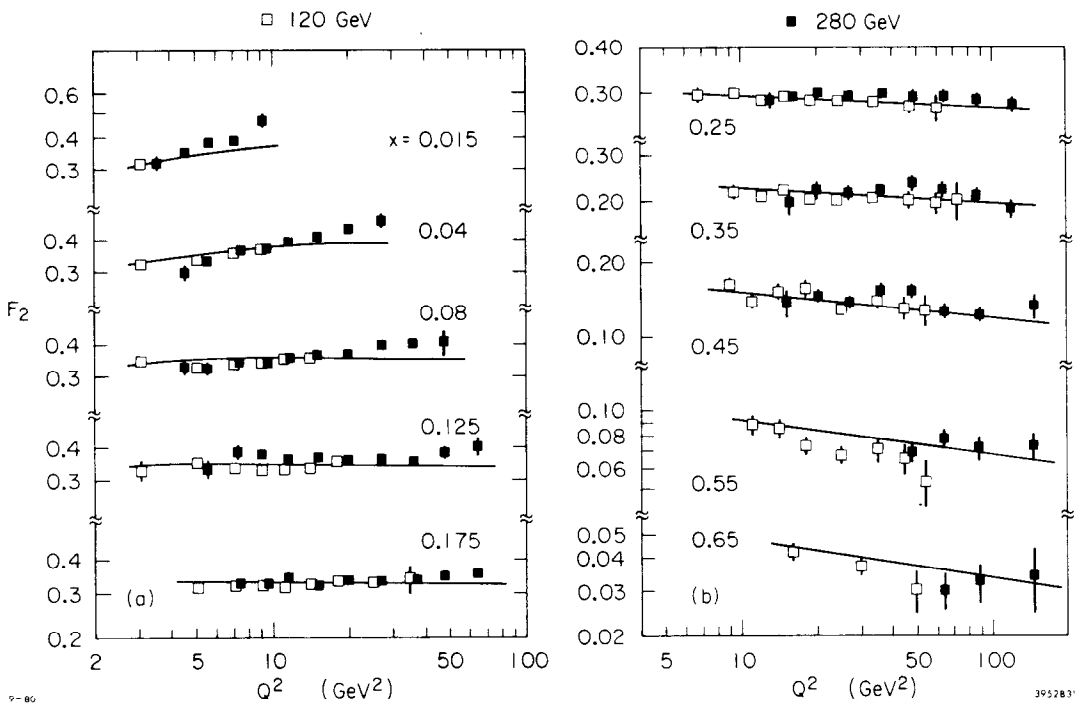

Fig. 35. The proton structure function F_2 from μp scattering versus Q^2 at various values of x.

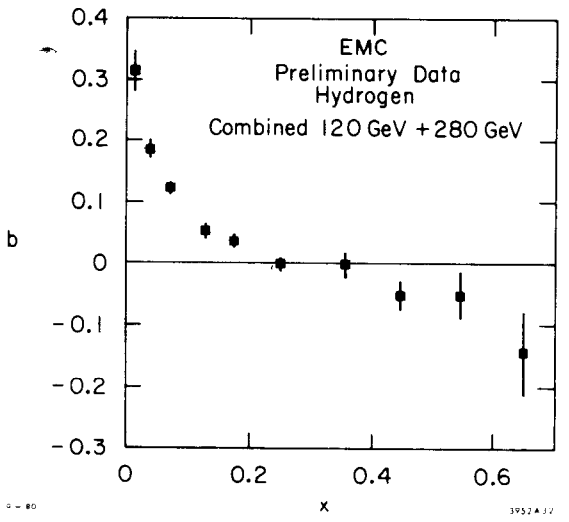

Fig. 36. The scaling violation parameter b versus x for μp scattering.

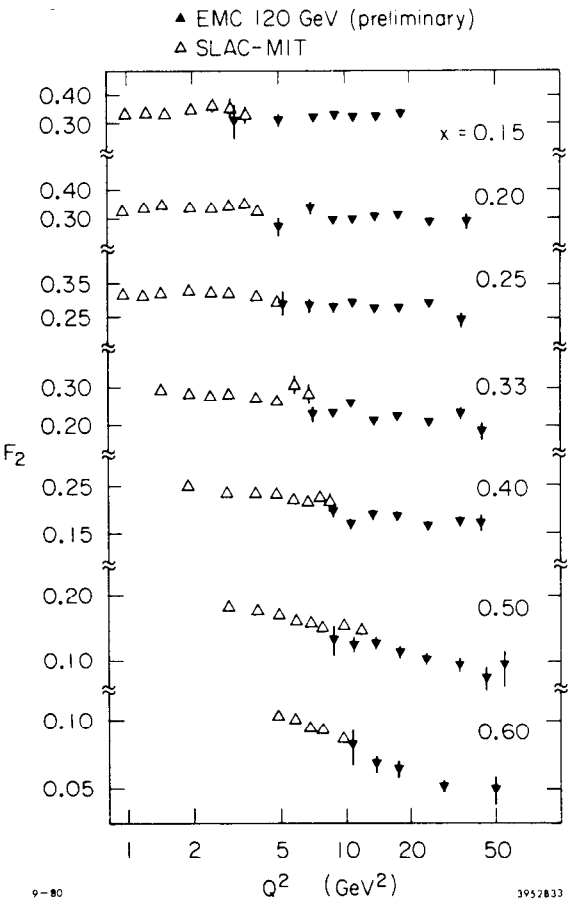

as Q^2 increases. The data come from 120 GeV and 280 GeV beam energies. The solid curves are QCD fits based on an analysis patterned after Abbott, Atwood and Barnett (described earlier) with second-order terms included (from Gonzales-Arroyo, Lopez and Yndurain[19]).

Figure 36 shows the slope parameter $b = d(\ell n\ Q^2)$ for the different bins in x. Clear evidence for scale-breaking is seen in these μp data, but not as dramatic as seen earlier in the SLAC ep and CHIP μp data, shown in Fig. 16. Figure 37 shows a comparison of normalization between EMC 120 GeV μp data and SLAC/MIT and SLAC data. The agreement appears to be quite good. Figure 38 shows the behavior of $F_2(x)$ for four values of Q^2, from 6 GeV^2 to 100 GeV^2. The dashed curves simply connect the points, and do not represent any theoretical calculation. The Fig. 38(d) shows these curves superimposed.

Fig. 37. Comparison of the structure function F_2 from μp and ep scattering.

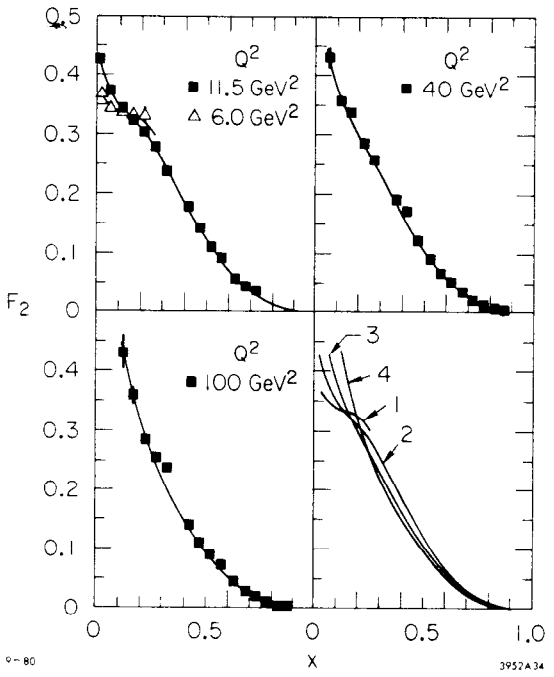

Fig. 38. Approximate behavior of F_2 from μp scattering. The solid curves, smooth fits to the data points, are shown in (d) for comparison.

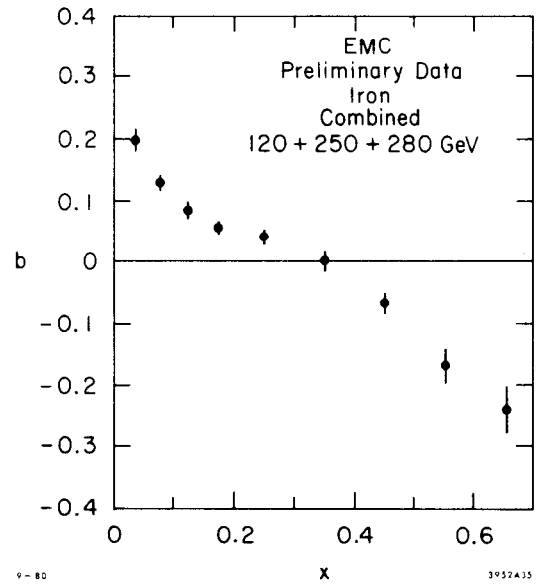

Fig. 39. The scaling violation parameter b for μ-iron scattering.

This is a beautiful example of the QCD-like scale-breaking features of the data, anticipated earlier in Fig. 11.

The EMC group also report on measurements of μFe scattering, where scale violations are also seen. The b parameter for μFe scattering is shown in Fig. 39.

The EMC group report QCD fits to these data with good χ^2, but with a value of Λ = .1 GeV. This smaller value of Λ corresponds to smaller scale-breaking parameter b seen in Fig. 35 compared to Fig. 16. The EMC group obtain good QCD fits to their data and the SLAC data by including power-law terms coming from higher twist operators, in apparent agreement with the analysis of Abbott, Atwood and Barnett.

C. The Bologna-CERN-Dubna-Munich-Saclay Collaboration (BCDMS)

Figure 40 shows the layout of the focussing toroidal detector of the BCDMS collaboration. The detector consists of an internal carbon target, 50-meters in length, and of ten super-modules of magnetized iron with eight layers of multiwire proportional planes and two layers of sequential trigger counters sandwiched inside. Data were taken for a range of Q^2 from 30 to 200 GeV^2, from incident beam energies of 120 GeV and 280 GeV. This experiment occupies the CERN NA4 area located downstream of the EMC experiment described earlier. BCDMS measure F_2 assuming a constant value of $R = .22$. A preliminary sample of data was reported in the summer of 1979, and is shown in Fig. 41. These data show no clear evidence of scale-breaking, but the preliminary nature of the analysis means one should await further publications, which should be forthcoming.

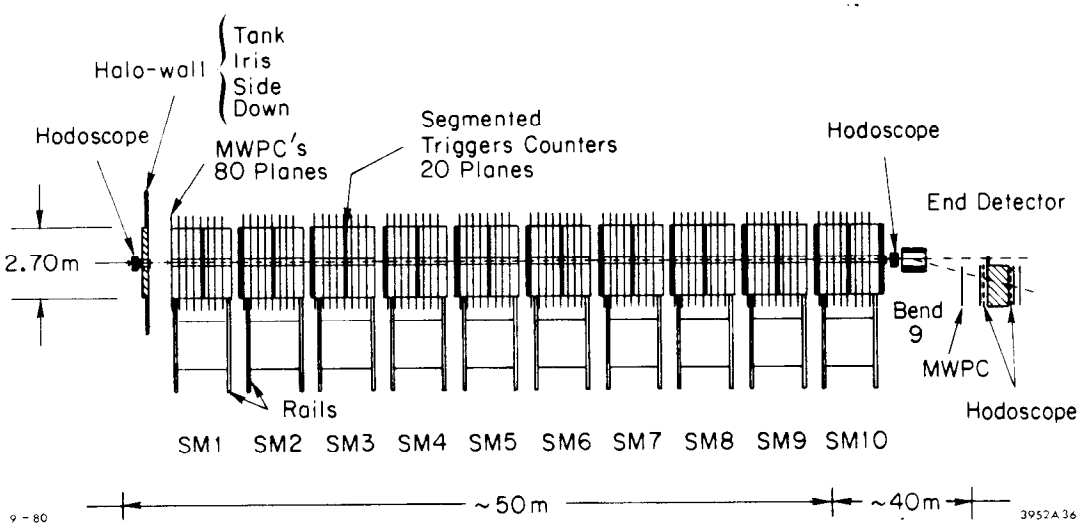

Fig. 40. Schematic layout of the BCDMS experiment at CERN.

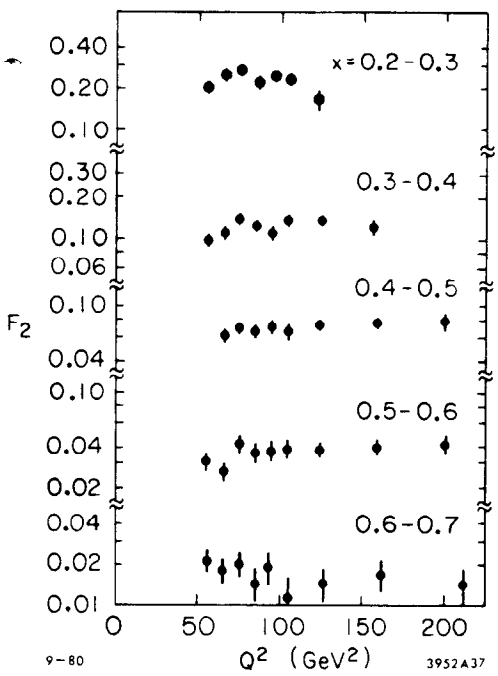

Fig. 41. Preliminary experimental values of F_2 from μ-Carbon scattering.

D. The Berkeley-Fermilab-Princeton Collaboration (BFP).

Finally let me mention one last high Q^2 experiment measuring cross sections for μ^+Fe inelastic scattering. Figure 42 shows an artist's view of an interesting magnetized iron detector. The difference between this detector and toroidal iron detectors is that there is no beam hole which causes acceptance uncertainties at small scattering angles. The detector consists of eighteen 25-ton magnetized iron modules, each 50 cm in length. The modules are instrumented with scintillators, drift chambers, and proportional counters. Data were taken at beam energies of 90 GeV and 209 GeV. The structure function F_2 was

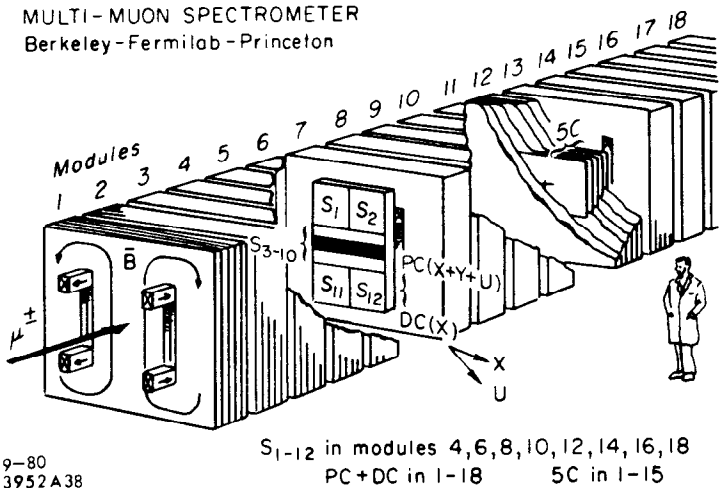

Fig. 42. Schematic layout of the BFP experiment at Fermilab.

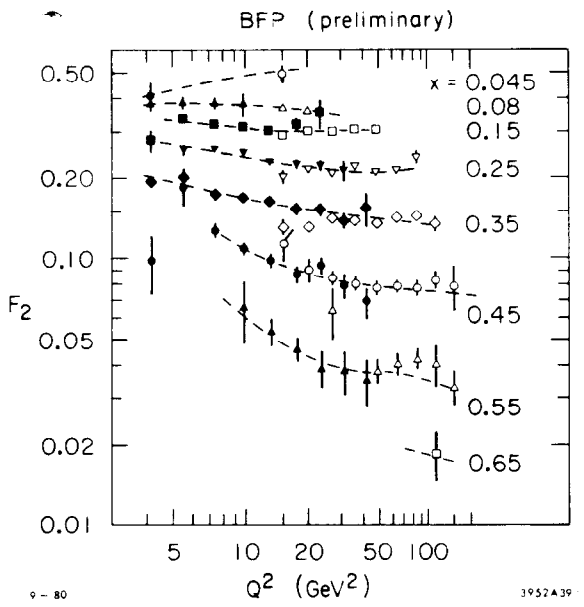

Fig. 43. Preliminary values of F_2 from μ-iron scattering. The dashed curves are not fits, but serve to connect the data points.

extracted from the data based on an assumed value of R. Figure 43 shows the preliminary results of F_2 presented at the 1979 Lepton-Photon Conference at Fermilab. The data show clear evidence of scale-breaking. The dashed curves in Fig. 43 are not fits, but are hand drawn curves to connect the points and show the trends of the data.

The BFP collaboration reported an 18% discrepancy in overall normalization between this data and the SLAC/MIT and SLAC data. This discrepancy lies outside quoted errors, and probably arises from some systematic effects not yet understood. Further analysis of the new BFP data may resolve this discrepancy. BFP also reports a considerable amount of multi-muon production data, which looks very interesting, but is a topic not considered here.

Clearly, the theoretical and experimental issues of deep inelastic phenomena continue to be in a state of change. We have seen the issue of scaling and the quark-parton model lead into a study of the strong interactions at a very fundamental level. The success of QCD tests is based on the validity of quark-parton model ideas, but modified to include gluon emission and quark-quark interactions in the hadronic piece of the process. Logarithmic scale breaking appears to describe well the data, but uncertainties in QCD calculations due to higher order terms and the uncalculated power law terms form higher twist operators cloud the present interpretations.

Further work on the side of the theory, and further high quality, high Q^2 data on the side of the experimenters may soon clarify the present uncertainties. But one expects the questions to continue to change, the data to continue to improve, and the interplay between the two to continue to be present. The future experiments will provide better control of systematic errors, smaller statistical errors and Q^2 ranges exceeding 1000 GeV^2 as we go to Tevatron energies and e-p storage rings.

I wish to acknowledge the considerable help from W. Atwood in the preparation of these notes, and the many useful discussions with him are especially appreciated. I also wish to acknowledge discussions with M. Barnett, H. DeStaebler and R. Taylor, likewise appreciated and helpful.

REFERENCES

1. R. P. Feynman, Phys. Rev. Lett. 23:1415 (1969); and R. P. Feynman, "Photo-Hadron Interactions," W. A. Benjamin, Reading, Mass., (1972).
2. J. D. Bjorken, Phys. Rev. 179:1547 (1969).
3. W. K. H. Panofsky, rapporteur's talk, in "Proceedings of the Fourteenth International Conference on High Energy Physics, at Vienna, Austria," CERN Scientific Information Service, Geneva, Switzerland, (1968) p. 23.
4. G. Miller, Ph.D thesis, SLAC Report No. 129 (1971); see also E. D. Bloom and F. J. Gilman, Phys. Rev. D4:2901 (1971).
5. M. Breidenbach and J. Kuti, LNS-MIT Report No. 247 (1971); see also O. Nachtmann, Nucl. Phys. B63:237 (1973).
6. C. G. Callan and D. J. Gross, Phys. Rev. Lett. 22:156 (1969).
7. G. Altarelli and G. Parisi, Nucl. Phys. B126:298 (1977).
8. C. F. Abbott, W. B. Atwood and R. M. Barnett, Phys. Rev. D22:582 (1980).
9. A. J. Buras and K. J. F. Gaemers, Phys. Lett. B71:106 (1977) and Nucl. Phys. B132:249 (1978).

10. J. G. H. deGroot, et al., Phys. Lett. B82:292 (1979);
J. G. H. deGroot, et al., Phys. Lett. B82:456 (1979);
J. G. H. deGroot, et al., Z. Phys. C1:143 (1979).
11. B. A. Gordon, et al., Phys. Rev. D20:2645 (1979).
B. A. Gordon, et al., Phys. Rev. Lett. 41:615 (1978).
12. A. J. Buras, Reviews of Modern Physics 52:199 (1980).
13. O. Nachtmann, op. cit.
14. D. W. Duke and R. G. Roberts, Phys. Lett. B85:289 (1979).
15. W. A. Bardeen, et al., Phys. Rev. D18:3998 (1978).
16. J. G. H. deGroot, op. cit.